5-27-2019

Scintillation Event Localization in Novel Hemi-Ellipsoid Detector for SPECT

Hanif R. Soysal
Louisiana State University and Agricultural and Mechanical College

SCINTILLATION EVENT LOCALIZATION IN NOVEL HEMI-ELLIPSOID DETECTOR FOR SPECT USING GEANT4

A Thesis

Submitted to the Graduate Faculty of the
Louisiana State University and
Agricultural and Mechanical College
in partial fulfillment of the
requirements for the degree of
Master of Science

in

The Department of Physics & Astronomy

by
Hanif Rauf Soysal
B.S., Louisiana State University, 2015
August 2019

Acknowledgements

First and foremost, I thank God, the One, the Almighty, who Sustains all, without whom none of my work would be possible. I am grateful for His ever-present Compassion and Guidance, by which I was able to successfully complete my research and from whom all my success comes. Furthermore, I thank my parents, who supported and guided me throughout my entire life and put up with me throughout my research.

No gratitude would be complete without acknowledging my advisor, Dr. Joyoni Dey. Her invaluable direction and support, coupled with her good-humored positivity and encouragement, made completing my research possible. My sincerest gratitude to Dr. Dey for her care, both in my research and as a mentor. Additionally, for their time, effort, and input, I would also like to thank my committee members Dr. Kenneth Matthews and Dr. Jeffrey Blackmon whose valuable advice proved much helpful.

The entire Medical Physics program here at Louisiana State University as well as the staff at Mary Bird Perkins Cancer Center have been instrumental in my education and training. The leadership of the program director, Dr. Wayne Newhauser, along with the mentorship of professors such as Dr. Kenneth Matthews, Dr. Jonas Fontenot, and many others have helped bring me to where I am today. My deepest gratitude goes toward all of them as I mention their names with warmth.

Finally, I thank my colleagues and friends for their assistance throughout my graduate studies, as well as their company, especially Cameron Sprowls and Bethany Broekhoven. Certainly, our friends are rays of light in our lives, and they made my time here a lot more cheerful than it would've been without them.

Table of Contents

List of Tables

List of Figures

Abstract

A high sensitivity Cardiac SPECT system using hemi-ellipsoid crystals with pinhole collimation was previously proposed by Dey et al. To investigate detector resolution for this design, the scintillation light spread on a monolithic hemi-ellipsoidal CsI crystal was simulated using Geant4 Monte Carlo. The expected distribution of scintillation light on the outer surface of the crystal from photoelectric absorption events was obtained from the simulations for selected points inside the crystal. Two sets of simulations were performed. For the first set, a look-up table (LUT) of 12 points was created and each point mapped to its expected light distribution—four points at each of the apex, the central region, and the base along one plane of the crystal, with each set of points situated at the corners of a "square" of side length 2mm. Algorithms were developed to localize test events by comparing the light distributions of the LUT points to that of the 5 test points in each region. The test points were also simulated as photoelectric absorption events. The results showed a visual differentiation between the light distributions of points in the central region and base, with the algorithms able to localize the test points in these regions to within a maximum of 1mm of where the events actually occurred. The apex exhibited worse performance with a maximum localization error of 1.5mm. In the second set of simulations, 1000 gamma ray interactions ("events") were simulated in different regions of the crystal (apex, central region, base); the light distribution from each event was compared to a new set of LUT points that were chosen to encompass the line of sight of the gamma rays. More than 99.5% of the gamma rays had localization errors of less than 3mm. In future, an LUT that covers the entire hemi-ellipsoid surface needs to be generated, which will allow a localization assessment over the entire detector system.

Chapter 1. Introduction

1.1. Background

In the United States, heart disease is the leading cause of death with about 630,000 deaths per year—about 1 in 4 deaths (Centers for Disease Control and Prevention, 2017). Heart disease also causes the US an estimated $200 billion dollars (Centers for Disease Control and Prevention, 2017).

To help diagnose heart disease as well as other problems with the heart, single photon emission computed tomography (SPECT) is used, an imaging modality that specifically gives functional information (National Institute of Biomedical Imaging and Bioengineering, 2016). SPECT is used widely in diagnostic imaging, with 17 million scans per year in the United States. Of these scans, about half are used for cardiac imaging specifically (Segall & Delbeke, 2011).

The procedure for acquiring a SPECT image begins with injection of a radioactive "tracer" into the body, which is then allowed to accumulate in the tissue or region of interest before being imaged with a gamma camera. A gamma camera consists of some type of collimation that can be attached at its end. The collimation serves to limit the direction that the photons come in, allowing the image to be reconstructed from the signals. Following the collimator is a scintillator, which produces large numbers of scintillation or optical photons around wherever a gamma ray interacts. The scintillation photons propagate through the crystal to an array of photosensors, such as large photomultiplier tubes (PMTs) or smaller silicon photomultipliers (SiPMs) or avalanche photodiodes (APDs). The signals are amplified, and an algorithm called Anger logic then decodes the interaction location by utilizing the relative signals from the different photosensors to aid

in reconstruction of the image (Alexander, 2016). A diagram of the procedure is illustrated in Figure 1. It should be noted that Anger logic works well for localizing the interaction location laterally, but not in depth, resulting in "depth of interaction" or parallax error and lowering resolution. This is not a big problem in flat detectors with parallel hole collimators since this contributes less to the loss in total detector resolution, but the effects are amplified in curved detectors without parallel collimation.

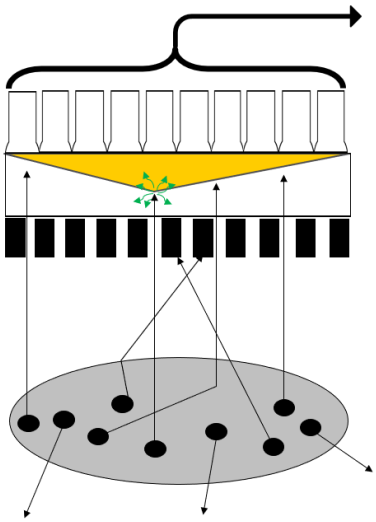

Figure 1. Diagram of SPECT procedure
Radioactive elements in the body emit gamma rays, some of which make it past a set of collimators and interact with a scintillating crystal, producing scintillation photons and lighting up photomultipliers. The signals are processed to generate an image.

However, there are some limitations to SPECT, including low spatial resolution and low sensitivity, resulting in larger administered doses and prolonged workflow (Bhusal, et al., 2019). As cardiac SPECT imaging is widely used for imaging of myocardial perfusion, ischemic effects, and abnormal heart wall motion, about 9 million patients undergo nuclear cardiac scans per year in the USA (Bhusal, et al., 2019) (Segall & Delbeke, 2011). While traditional or first-generation SPECT imaging systems used Anger logic on parallel hole collimators, many improvements to cardiac SPECT have been achieved since in "second

generation" SPECT. These newer generation cardiac imaging systems such as GE Discovery and DSPECT have been able to achieve improved sensitivity from traditional gamma cameras using anger logic by a factor of 5 to 8 by utilizing different configuration geometries (such as placing cameras closer to the organ for dedicated cardiac imaging), better reconstruction and localization algorithms, and better detector hardware (Slomka, Pan, Bermand, & Germano, 2015) (Garcia, Faber, & Esteves, 2011) (Iwata, et al., 2001) (Seo, Mari, & Hasegawa, 2008) (Madsen, 2007) (Slomka, Patton, Berman, & Germano, 2009) (Erlandsson, Kacperski, Gramberg, & Hutton, 2009) (Volokh, Lahat, Binyamin, & Blevis, 2008). This has resulted in improvements visible in cost, processing time, spatial resolution, sensitivity, and detection efficiency (Seo, Mari, & Hasegawa, 2008).

One such advancement has been proposed by Joyoni Dey's group. Dey previously proposed a system for cardiac imaging using 21 hemi-ellipsoid detector modules, shown in Figure 2. Assuming a 3mm localization error in the crystal, this design can achieve 3x better sensitivity than second generation SPECT systems (or about 15 times traditional SPECT systems) (United States Patent No. 8519351B2, 2010) (Dey, 2012) (Bhusal, et al., 2019). Because the system utilizes pinhole collimators, the size of the pinhole can be adjusted to trade off the improved sensitivity for improved resolution. The higher sensitivity can also be traded off for different acquisition protocols e.g. low dose vs faster acquisition. The benefit of the system comes from the use of curved hemi-ellipsoid crystals, the geometry of which is shown in Figure 3. The configuration allows for a larger detector area by utilizing the curved nature of the separate detector modules which yield more compact packing. Furthermore, the pinhole collimator increases magnification in the apex region of the curved detectors. Although the proposed system has been shown previously to provide

considerable improvements over existing cardiac imaging systems, the application is not limited only to cardiac imaging. Different configurations of the same detector elements can potentially improve imaging of other organs.

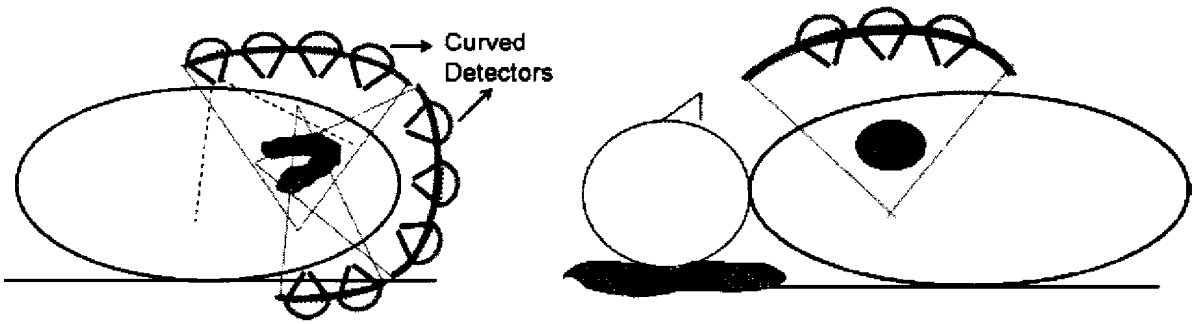

Figure 2. A detector system for cardiac imaging proposed by Dey group
In the diagram on the left, a transverse view shows nine of the hemi-ellipsoid detector elements arranged in an arc. In the sagittal view on the left, the diagram shows three such arcs arranged around the heart. From (United States Patent No. 8519351B2, 2010)

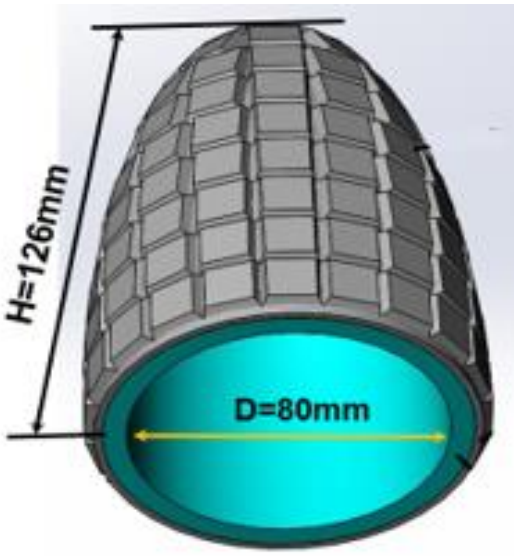

Figure 3. Depiction of a hemi-ellipsoid detector module
Shown here is the proposed curved hemi-ellipsoid detector made from a scintillator and photosensors. From base to apex, the length is 126mm along the central axis. The hollow circle at the base of the crystal is 80mm wide in diameter. The crystal is 6mm thick at the base and at the apex. Small photosensors are shown tessellated onto the surface of the detector module. The photosensors may be SiPMs or APDs when manufactured.

The purpose of this study is to investigate the assumption of a localization error of 3mm for the hemi-ellipsoid design, by determining the achievable localization error in the curved detector. Localizing to a general area near the surface of the crystal (e.g. whether the interaction happened in the apex, mid, or base region) is expected to be easier than subsequently identifying of the depth of the interaction. However, even for depth of interaction, the curved nature of the detector modules will provide an advantage in localizing scintillation events, because of the potentially larger discriminating light-distribution for different depths of scintillation events as shown in Figure 4. Determination of depth of interaction is important to overcome the non-negligible parallax error that results with curved crystals using pinhole collimation.

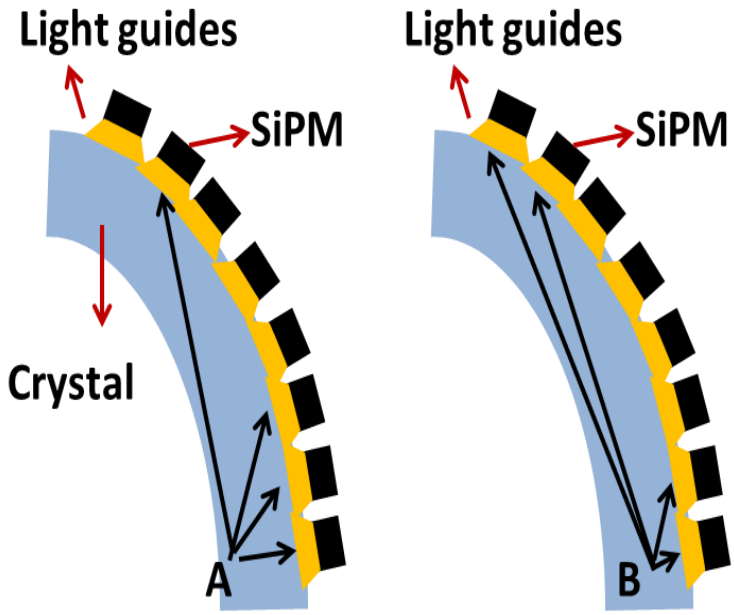

Figure 4. Diagram of two scintillation events at different depths
The scintillation events, A and B, are at two depths along the same normal of the crystal. Notice that an event that occurs at point A will not deposit much light farther up the crystal, due to the limited line of sight, whereas an event that occurs at point B can be expected to deposit more light on the photosensors near the apex. By utilizing such information, it is hoped that the curved nature of the crystal will allow for better localization of events, and thus higher resolution.

1.2. Project Overview and Hypothesis

Prior work with the hemi-Ellipsoid detector system showed that the system can achieve three times the sensitivity than second generation SPECT systems, assuming localization error in the detector of 3mm. Our hypothesis in this work is that this localization error of 3mm or less is possible.

The method that employed to achieve this resolution is through searching of a Look-up Table (LUT) of scintillation light distribution, for surface and then depth of interaction localization. No doubt, when an interaction occurs inside the crystal, the intensity distribution on the photosensor array at the surface of the crystal will uniquely vary according to where in the crystal the interaction occurred. For example, an interaction that occurs in the crystal near the apex of the hemi-ellipsoid, along the central axis, will heavily light up detectors near the apex and leave detectors near the base devoid of light. It is expected that different interactions that occur at the same point in the crystal will result in highly similar intensity distributions in the detector array Therefore, by knowing what the intensity distribution looks like for an interaction that occurs at a particular point *P*, if we later obtain a distribution that very closely resembles it, we will know that the interaction must have occurred very near *P*. The closer the resemblance, the closer we can pinpoint the true location of the unknown interaction. The goal then was to systematically simulate interactions at various points in the crystal and record the average intensity distribution that results on the photosensor arrays. This mapping of crystal points to intensities on the scintillation light photosensor arrays (such as APDs or SIPMs) will form our LUT. Later, when interactions occur at random, unknown locations in the crystal, we can use the LUT to localize where the interaction occurred by obtaining the entry in the LUT whose intensity

distribution most closely resembles that of the incoming random interaction. Our expectation was that the curvature of the hemi-ellipsoid would allow for adequate discrimination, and provided we construct a high-enough resolution LUT, we would be able to achieve localization within 3mm, as hypothesized. A summary of this approach is illustrated in Figure 5.

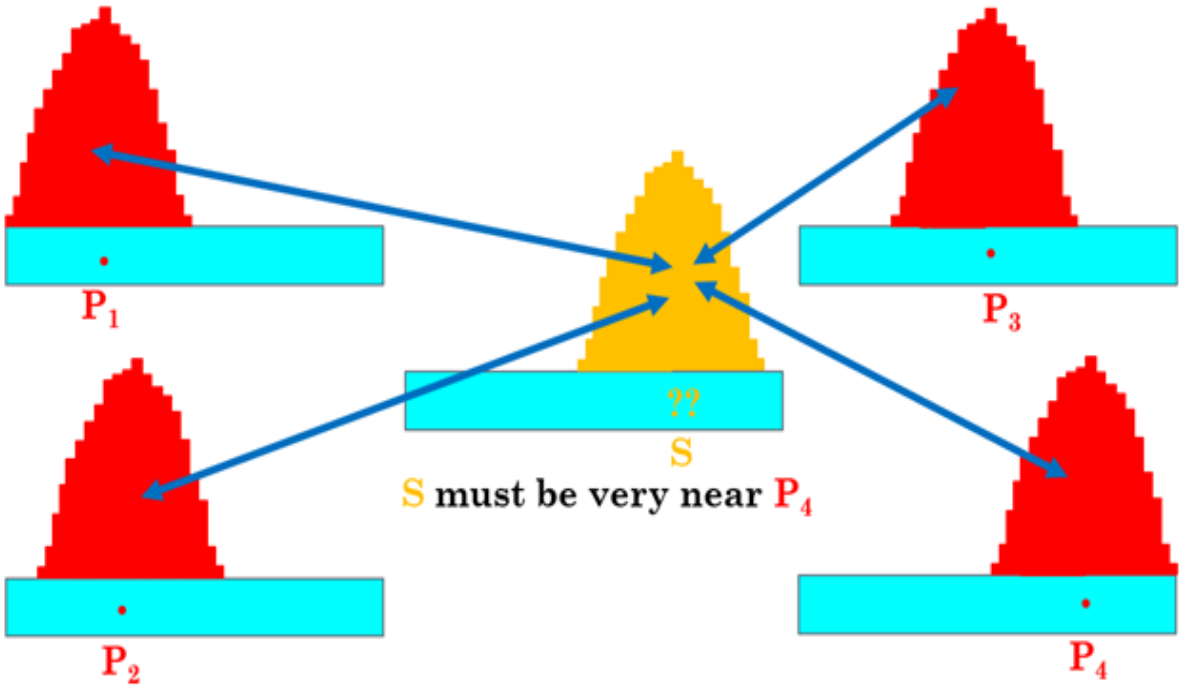

Figure 5. Example depiction of LUT approach
In this example scenario, four points exist in the LUT, points P1 through P4, at different locations in a flat scintillating crystal. An event at each of these locations might produce the scintillation light patterns shown as histograms above the crystal. Later, when an experimental light pattern is obtained via the photosensors, the light pattern can be compared to the light patterns in the LUT, with the best match(es) allowing us to localize the simulated/experimental light pattern, in this case allowing us to determine that the experimental event must have occurred near P_4.

The viability of this method depends on the distinguishability of the intensity distributions of the simulated crystal points. To initially show the feasibility of this approach, we performed a deterministic simulation using MATLAB to see if there are observable

differences in the intensity distributions of nearby points. This is described in Chapter 2, Preliminary Feasibility Study.

Subsequently, we developed a localization algorithm, ran Monte Carlo simulations, and assessed the results. These efforts were divided into three specific aims (SA):

1. SA1: Monte Carlo simulation of hemi-ellipsoid detector using Geant4 (Chapter 3).
2. SA2: Development of localization algorithms (Chapter 4).
3. SA3: Validation and verification (Chapter 5).

Following the discussions on specific aims, we finish the main section of this work with Chapter 6, Conclusions. The Bibliography and Vita then follow.

Chapter 2. Preliminary Feasibility Study

2.1. Overview

A preliminary investigation was performed to demonstrate feasibility of the hypothesis before performing simulations in Geant4. This investigation employed a deterministic simulation, implemented using MATLAB. For 3 pairs of points chosen at the apex, base, and central regions of the crystal at different depths (Figure 6), a scintillation event was simulated by generating isotropically emitted light rays which were then traced until they reached either the outer surface of the crystal (reached the plane of the photosensors) or the inner surface of the crystal, as shown in Figure 7.

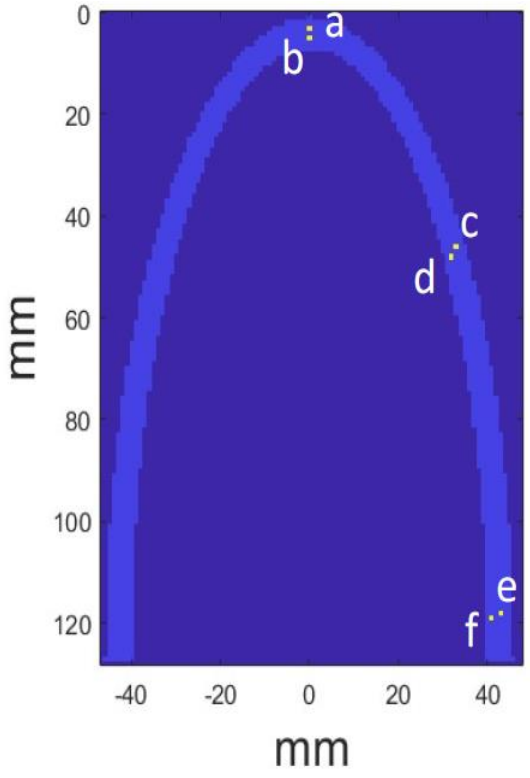

Figure 6. Location of the three pairs of points used in the deterministic simulation of the isotropic emission of rays

.

Since the inner surface of the crystal will be a (diffuse) reflective surface, the same process was applied to the voxels along the inner detector—the intensities recorded were

treated as points and rays were re-emitted isotropically from the inner surface until they hit the outer detector surface as shown in Figure 7. Intensities were recorded for this outer crystal surface, i.e. where the photosensors are expected to be, all the while accounting for the $\frac{1}{r^2}$ fall-off of intensity as well as Lambert's cosine law, as detailed in Figure 7.

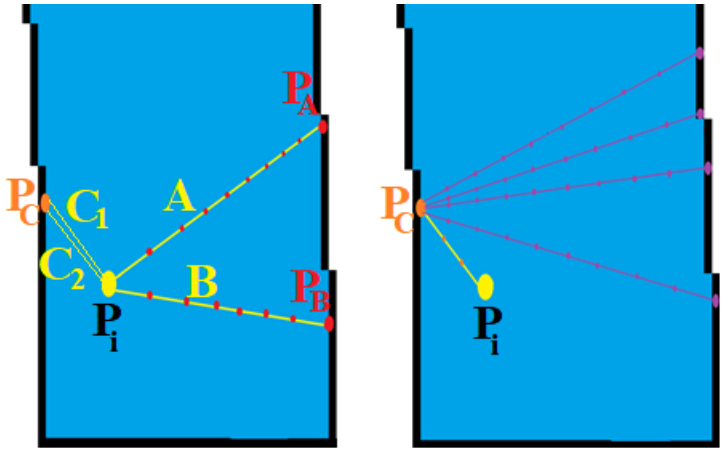

Figure 7. Trace of rays emitted isotropically hitting either surfaces of the crystal
Rays are emitted isotropically from each of the chosen points and observed at every 1mm increments to check whether the ray is still in the crystal. As shown on the left image, for every point P_i, a ray is stopped if it hits the outer surface of the crystal and recorded. In the example in the image, rays A and B produce some intensity at the matrix elements located at P_A and P_B in a matrix called *OuterIntensities*. If, however, the ray hits the inner surface of the crystal, the intensity is recorded, as in rays C_1 and C_2 being recorded at point P_C in a matrix called *InnerIntensities*. Afterward, all of the elements in the *InnerIntensities* matrix will then be re-emitted as shown in the image on the right, utilizing Lambert's Cosine Law to adjust for the intensity. For the sake of computation speed, we accumulate the light on the inner surface and re-emit isotropically only once for each point on the inner surface. The reason that both rays C_1 and C_2 produce a count at the same point is due to the resolution of the simulation, namely that the elements of the matrices used to represent the points are considered to be 1mm apart, allowing for multiple rays from a source to hit the same point on the crystal's surface.

2.2. The Use and Generation of "Masks"

The simulation of light waves was implemented using "masks" to represent the different regions of the geometry. A matrix was created with dimensions of 128mm x 96mm x 96mm, matching the size of the hemi-ellipsoid. The crystal was "drawn" into the matrix by using the equation for an ellipse. More specifically, let a_i, b_i, and c_i denote the principal semi-

axes of the inner surface of the crystal; a_o, b_o, and c_o denote the principal semi-axes of the outer surface of the crystal; i, j, k denote the indices of a matrix element (and thus a location); and o_x, o_y, o_z denote the origin of the hemi-ellipsoid. Then consider the following equations of two ellipses:

$$Value_{inner} = \left(\frac{i-o_x}{a_i}\right)^2 + \left(\frac{j-o_y}{b_i}\right)^2 + \left(\frac{k-o_z}{c_i}\right)^2 \quad (2.1)$$

$$Value_{outer} = \left(\frac{i-o_x}{a_o}\right)^2 + \left(\frac{j-o_y}{b_o}\right)^2 + \left(\frac{k-o_z}{c_o}\right)^2 \quad (2.2)$$

No doubt, when $Value_{inner} = 1$, this represents the inner surface of the ellipse, and $Value_{outer} = 1$ represents the outer surface of the ellipse. Matrix elements whose indices produced a $Value_{inner} < 1$ were considered to be the hollow inside of the ellipsoid. These matrix elements were changed to 0. Matrix elements for which the indices produced a $Value_{outer} > 1$ were considered to be outside and away from the ellipse, and the value of these elements in the matrix was changed to 0.01. All other matrix elements were given a value of 1, denoting that they are a part of the crystal. Finally, A layer was concatenated to the bottom of the matrix with each of its elements also having a value of 0. This complete matrix was then ready to serve as our "mask". The values of the matrix elements are summarized in Figure 8.

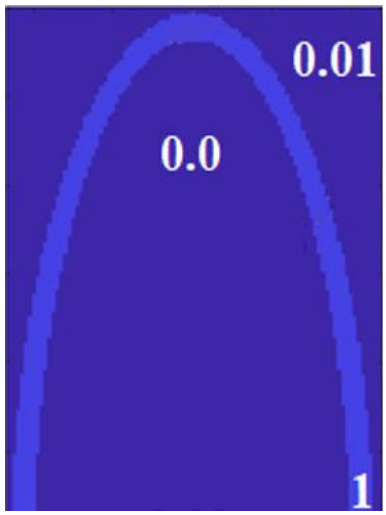

Figure 8. Values assigned in masks to the different regions of the geometry
A value of 1 represents matrix elements that form the inside the crystal. A value of 0.01 represents values outside of the crystal. A value of 0.0 represents values on the inside of the crystal. Finally, a value of 0.02 is assigned to the bottommost row of the matrix.

2.3. Method for Deterministic Simulation

For each of the chosen points discussed in section 2.1 and shown in Figure 6 above, rays of "scintillation photons" were simulated isotropically: a spatial resolution of 1mm and an angular resolution of 1° were used. That is, for each of the 6 points, rays of "light" were propagated outward at every 1° (azimuthally and polarly) and traced in 1mm steps, and each ray was terminated upon hitting a surface of the crystal (i.e. when the value of the element nearest to the location of the ray at each 1mm increment was no longer equal to 1, as values of 1 denote the crystal). Near identical outputs were observed for steps finer than 1mm, justifying our use of 1mm steps to speed up the deterministic simulation.

When a ray was terminated, its intensity was recorded via accumulation in the matrix element where the termination occurred. Therefore, the matrix elements that surround the crystal is used to record how many rays have hit that element. All rays start

with an intensity of 1. That intensity is decreased by a factor of the square of the distance between the point of propagation and the location where it hit the crystal.

Recording the intensities is done in three separate matrices. These matrices have the same dimensions as our mask with all of the elements possessing counts of 0. The first of these records termination of rays that travel directly from the propagation point to the outer surface of the crystal. We'll call this *OuterIntensities*. The second records termination of rays that travel directly from the propagation point to the inner or bottom surfaces of the crystal. This shall be termed *InnerIntensities.* Finally, the third matrix records termination of rays on the outer surface of the crystal, but that are generated via reflection of light from the inner surface of the crystal to the outer surface (as discussed in the following paragraph). This will be named "*OuterReflectedIntensities*".

The diffuse (Lambertian) reflection of light from the inner surface of the crystal outward (as shown previously in Figure 7) is performed similar to the isotropic propagation of the light for each point. It is performed in bulk (for computational purposes), after all direct rays of light have hit any surface of the crystal. Essentially, each voxel in *InnerIntensities* which has some nonzero intensity now becomes the new "points" from which isotropic rays are traced until they hit the outer edge of the crystal. The same algorithm that was run for each of the six crystal points is reused for each nonzero voxel along the inner surface of the crystal with two additions: first, for a particular point, the intensity of each ray did not start with 1. Rather, the initial intensity of each ray was equal to the value of the matrix element at that position (recall that counts were being accumulated in *InnerIntensities* in the first step. Depending on how many counts hit a particular voxel, and how far that voxel is from the initial point of propagation, the

intensity may be greater than or less than 1). Secondly, Lambert's cosine law (which states that when light is reflected from a diffuse reflector, the intensity of the light is proportional to the dot product of the surface's normal and the direction of the incident ray) was applied by multiplying the intensity by the dot product of the two directional unit vectors n and m, where n is the unit vector in the direction of propagation and m is the unit vector in the direction of the new voxel that the reflected light travels (Weik, 2000). As before, the $\frac{1}{r^2}$ fall-off with distance was also accounted for. The resulting intensity, upon hitting the outer surface, was recorded in *OuterReflectedIntensities*.

Two separate matrices, *OuterReflectedIntensities* and *OuterIntensities*, were used only for debugging and verification purposes and to have the data available separately for possible future use. The two matrices were added together to obtain the simulated final intensities on the outer surface of the crystal—the intensity from both direct ray tracing from the point of propagation as well as the intensity from reflection of ray tracing

2.4. 2D Visualization of Intensities on Surface of 3D Ellipse

Visualization of the 3-dimensional intensity distribution was done in 2-D. A cut was made at the 180 deg longitude, diametrically opposite points being considered on the zero-degree longitude as shown in Figure _ and the ellipsoid was opened up. The intensities were then mapped out. The number of samples was changed height-wise (top to bottom) to maintain a uniform sampling of the circumference. Figure 9 shows a crystal with uniform intensity in all of its voxels opened up.

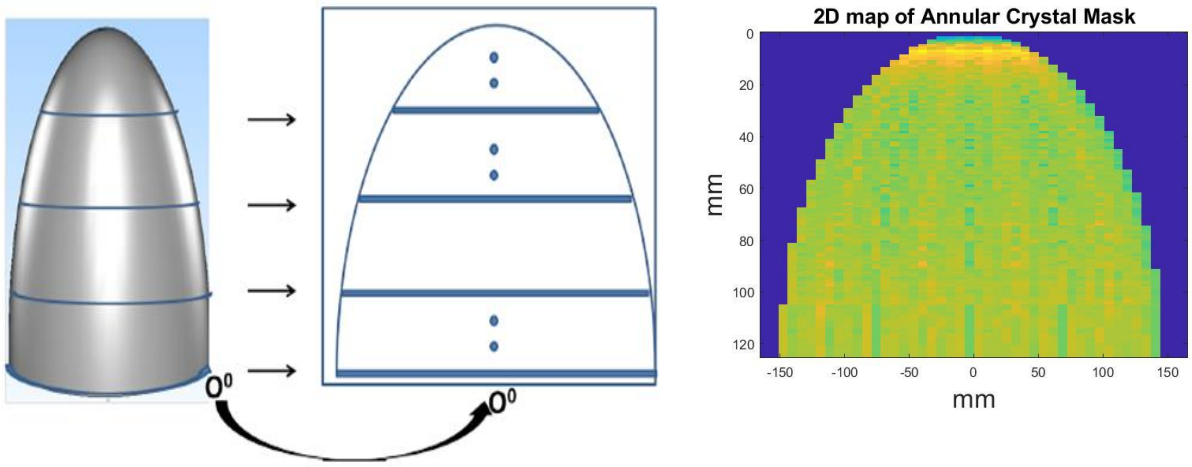

Figure 9. Depiction of 2D visualization of 3D masks
A cut is made at an arbitrary plane defined by the 0° point and the central axis (left). The ellipsoid is opened-up and the intensities along the circumference are mapped out into rows, displayed in a 2D map (right). Shown here is a 2D map of intensity.

2.5. Results and Conclusion

Figure 10 (A-F) shows the results of this preliminary feasibility work. The opened-up intensities are shown for the three pairs of points. When comparing the light patterns for the pairs, the differences are clearly ascertainable visually, especially for pairs C-D and E-F (for example, in the tails at the ends of the light pattern or in the intensity of the central area of the pattern). The difference is slightly less obvious for points A and B, although point B still has a longer tail. It is worth noting here that the pairs of points were apart by 2 mm for pair A-B or $\sqrt{5}$ mm ($\sim$ 2.3 mm) for pairs C-D and E-F. Our results are encouraging as "scintillation events" occurring at these pairs of points 2-2.3 mm apart in the crystal are able to be distinguished visually, indicating that a more detailed assessment with Monte Carlo Simulations is warranted.

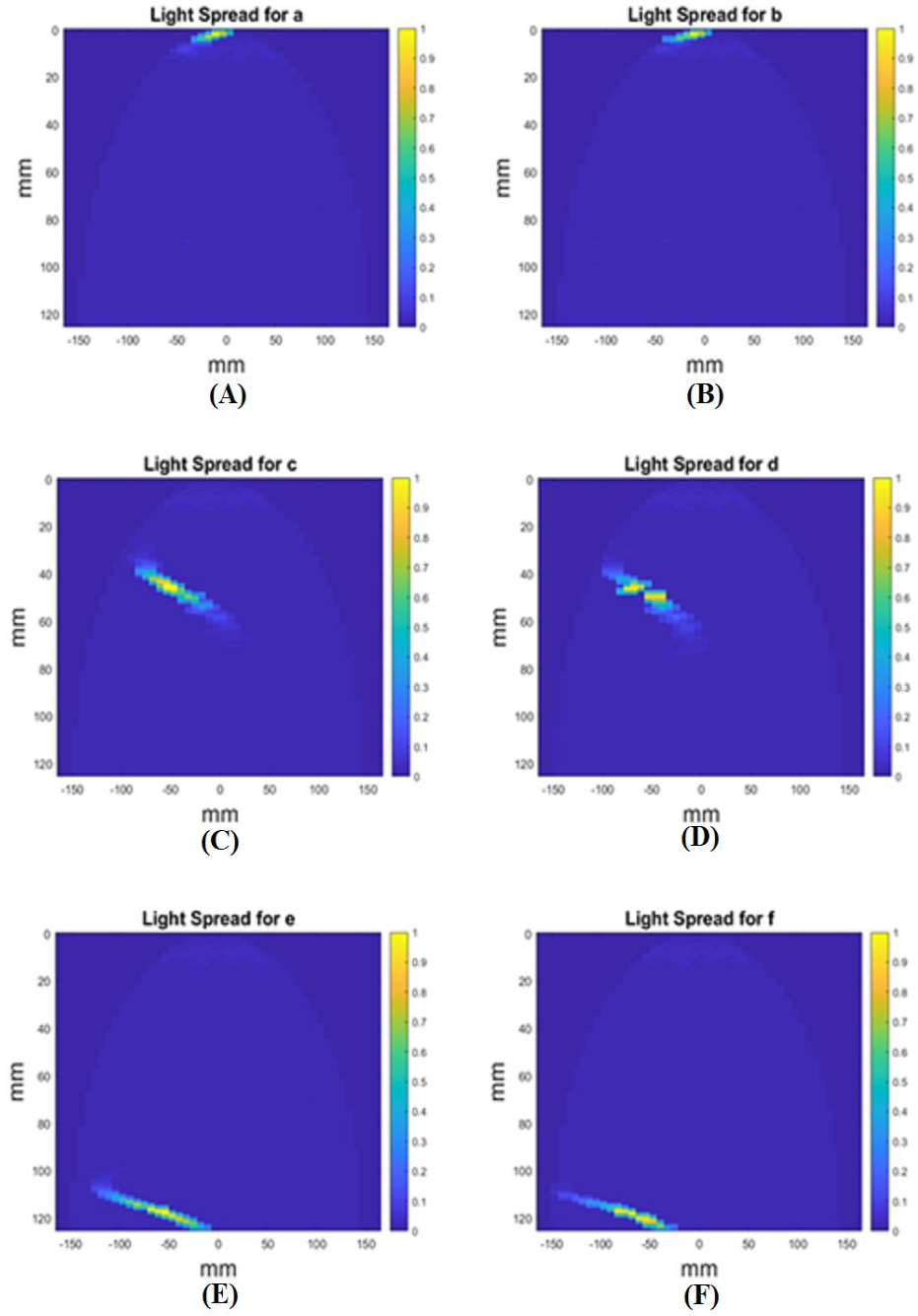

Figure 10. Results of feasibility study for the six simulated points

The fact that the points are visually distinguishable from each other shows that they can theoretically be computationally differentiated. Monte Carlo simulations should help the differentiability.

One drawback of this feasibility study was the inherent limitation in discretizing a continuous process. A matrix was used with essentially a 1mm resolution (the distance

between elements in the matrix), and so the simulations are limited to 0.5mm of precision. (A ray whose coordinates hit the ellipsoid at the middle of two matrix elements will be recorded in one or the other matrix element. Since the resolution of the matrices, or masks, is 1mm, a ray hitting in the middle would at most be off by 0.5mm). Since this drawback is not expected in Monte Carlo simulations which track photons continuously without being constrained to a grid of matrices, we expect Monte Carlo simulations will allow even further differentiability (and thus localization). Also, no quantification of the differentiability of light distributions was performed in the feasibility study. To show feasibility, being able to visually distinguish distributions was deemed satisfactory. With this success, we move on to a non-deterministic simulation in Chapter 3 Aim 1: Monte Carlo Simulation to Generate LUT Points Using Geant4.

Chapter 3. Aim 1: Monte Carlo Simulation to Generate LUT Points Using Geant4

This chapter details the simulation process in Geant4, providing a detailed walkthrough of the simulation procedure, the generation of points that need to be run for the simulation, as well as the procedure by which the simulations were done on high performance computing (HPC) clusters.

3.1. Monte Carlo Simulation

We used Geant4 Monte Carlo to simulate the illumination of the outer surface of the CsI crystal by scintillation events that occurred at various chosen points in the crystal (S. Agostinelli et al., 2003). The following Physics processes associated with optical photons were enabled: optical absorption, optical Rayleigh Scattering, Scintillation, Cerenkov, Decay, Compton Scattering, Photoelectric Effect, Ionization, Bremsstrahlung, Diffuse Reflection, as well as other default physics processes (which were not used in the simulation). To be able to control the location where a scintillation event occurred, we simulated photoelectric absorption events at the chosen points, instead of shooting gamma rays directly into the crystal and having them interact at random locations along a path. We did this by considering that the absorption of a 140.5 keV gamma-ray would produce on average 9132 photons (Knoll, 2010). For each of the points used to create the LUT, 1000 such scintillation events were simulated, for a total of 9,132,000 photons emitted isotropically at each point. (In actuality, an average of 9,111,074 with a standard deviation of 950 photons were recorded, meaning some of the 9,132,000 photons did not reach the detector.)

The crystal was constructed as a hemi-ellipsoid shell (further referred to as simply "ellipsoid"). The outer surface of the crystal had major axes in the X and Z directions of

46mm and inner axes of 40mm (so that the crystal was 6mm thick at the base. The outer surface of the crystal extended to a height of 126mm at the apex and the inner surface extended to 120mm (again, so that it is 6mm thick at the apex). A secondary "photosensor" or ellipsoid shell was created on top of the existing crystal ellipsoid for the actual detecting of the incoming photons. The passing of the photon into this new detecting medium was considered a detection event and the simulated scintillation photon was stopped upon entry into this detecting medium. A small ring was created at the base of the crystal to act as a reflective coating for the base so that photons hitting the bottom edge of the crystal were reflected. The geometry produced in Geant4 is shown in Figure 11 (with scintillation photons created near the base on bottom right shown in green).

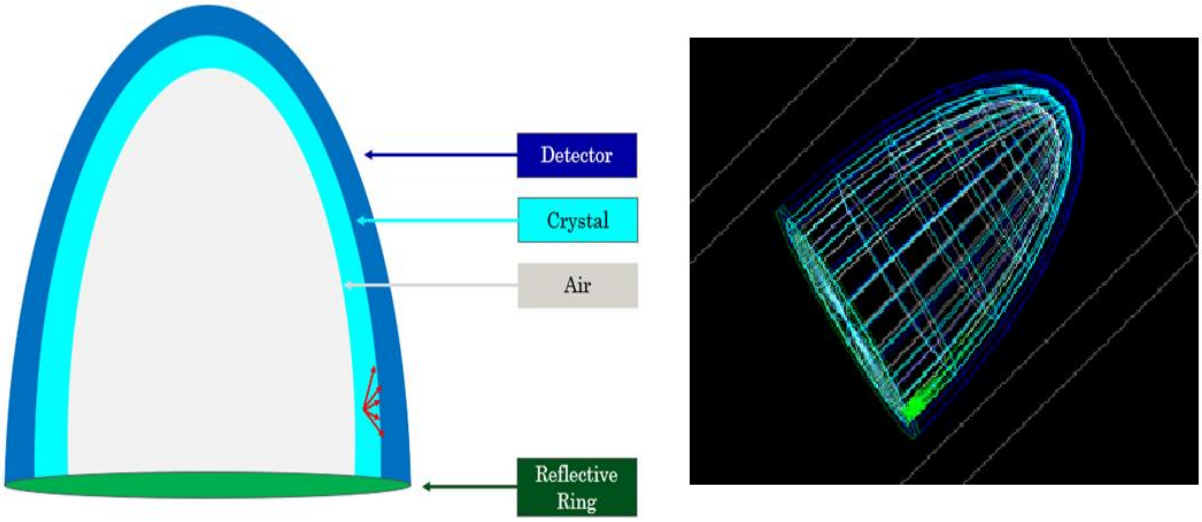

Figure 11. Hemi-Ellipsoid Detector Geometry in Geant4
The Dark blue ellipsoid represents the photosensors, i.e. the detecting element, the cyan represents the crystal, and the white represents the inside of the ellipsoid. A green ring at the bottom is present for reflection from the bottom edge of the crystal. At the bottom of the image, the paths of scintillation photons in the crystal being simulated are shown.

For the simulation, the UNIFIED model was used with a dielectric-dielectric surface (as this represents the CsI-to-epoxy surfaces of the photosensor elements) and a dielectric-

metal surface (as this represents the CsI-to-reflective-coating on the inner surface and base of the crystal). The surface between the crystal and the outer photosensors were set with a "ground" finish, and the base and inner surface of the crystal were set to "groundteflonair" to mimic the reflective coating. The crystal was modeled by setting its material to containing 99.6% CsI and 0.4% Tl (N. Grassi, 2008). A refractive index database was used to obtain the refractive indices at the desired energies, which cites the Journal of Physical and Chemical Reference Data (Polyanskiy, 2018) (Li, 1976). The scintillation photon used for the simulation were obtained from previous example simulations used in the Geant4 tutorials (CERN, 2018). Data from CERN's Crystal Clear Collaboration was used to obtain the absorption lengths of the crystal at various energies (Gentit, 2007). To obtain the energy-frequency distribution produced by the scintillation of a 140.5keV gamma ray in CsI(Tl), a plot from Saint-Gobain's website was used, which was digitized via an automatic plot digitizer (Saint-Gobain, 2007) (Rohatgi, 2019). Reflectivity for the crystal was set to 100% diffuse reflection, and the other types of reflection were disabled as they were seen as irrelevant for the purposes of this simulation. [The values for the different types of reflection were actually varied, but it was seen as having no visible effect on the outcome.]

The Z-axis of the crystal goes through the geometric center of the full ellipsoid and the very rip of the apex. The X- and Y- axes form the plane which encompasses the base of the crystal.

3.2. Generation of Points for Developing LUT for Verification of the Scintillation Photon Simulation

To precisely obtain low localization error, the LUT sampling must be finer/smaller than the desired localization error. To achieve this, we first limited ourselves to a single, central slice of the crystal on the YZ plane at X=0. This is justified because rotational

symmetry can be used to obtain the expected intensity distribution for crystal points that occur in different slices. Choosing the central slice allows us to obtain the largest possible cross section. Furthermore, only half of that slice was used for simulating LUT points, cut off at the apex, again invoking rotational symmetry.

After the geometry was restricted, we chose points along the outer surface of the crystal that were 1mm apart from each other (Euclidean distance). At each of these points along the outer surface, a normal was calculated, and further points were obtained by going into the crystal by distances of 1mm along the normal at these points. Effectively, this ensured that each point in the crystal is at most 1mm away from the neighboring points. The full set of points that will eventually need to be simulated along one slice is shown in Figure 12. There were 715 such points.

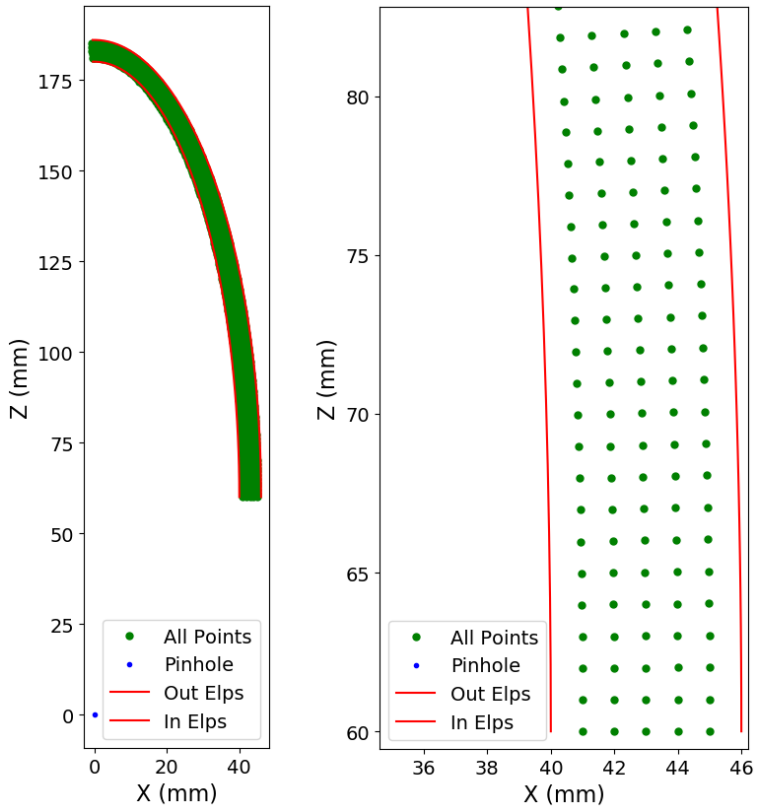

Figure 12. All LUT points that need to be generated in the central slice of the crystal
Left: All points in main slice. Right: Zoomed-in image.
A small padding on the inner ellipse is used to ensure points aren't too close to the edge. The location of a hypothetical pinhole is shown at the origin.

For the scope of the direct simulation of scintillation photons (see section 5.2), a subset of those points was chosen to produce working algorithms for binning, localization, and matching (as discussed in Chapter 4 Aim 2: Localization Algorithms). The points were chosen at three locations on the hemi-ellipsoid—the base, central region, and apex as shown in Figure 13. At each of the three locations, four points were simulated from the pool of LUT points determined in the first step. These four points were chosen in a square-like shape so that they are about 2mm apart from each other.

After choosing these four LUT points, five test points were also determined, one test point in the center of the four LUT points, and four test points closer to one of each of the

four LUT points. If we let the four LUT points in any one of the regions be defined by (x_1, y_1), (x_2, y_2), (x3, y3), and (x_4 , y_4) then the coordinates of the remaining 4 test points are given by

$$\frac{1}{6}\begin{bmatrix} x_1 + x_2 + x_3 + 3x_4 & y_1 + y_2 + y_3 + 3y_4 \\ x_1 + x_2 + 3x_3 + x_4 & y_1 + y_2 + 3y_3 + y_4 \\ x_1 + 3x_2 + x_3 + x_4 & y_1 + 3y_2 + y_3 + y_4 \\ 3x_1 + x_2 + x_3 + x_4 & 3y_1 + y_2 + y_3 + y_4 \end{bmatrix}$$

Thus, the coordinates of the remaining four test points are a weighted average of the LUT points given by the following matrix operation:

$$\frac{1}{6}\begin{bmatrix} 1 & 1 & 1 & 3 \\ 1 & 1 & 3 & 1 \\ 1 & 3 & 1 & 1 \\ 3 & 1 & 1 & 1 \end{bmatrix}\begin{bmatrix} x_1 & y_1 \\ x_2 & y_2 \\ x_3 & y_3 \\ x_4 & y_4 \end{bmatrix}$$

Recall that the four LUT points in each region formed a rough square-like shape with the distance between adjacent points roughly equal to about 2mm. The four remaining test points generated by the matrix multiplication method above themselves form a square-like shape that is an offset of the four LUT points, with the distance between adjacent points equaling roughly $^2/_3$ of a millimeter. The four LUT points and five test points described are shown in Figure 13 for the central region. These test points, just like the LUT points, are simulated as if a photoelectric absorption event occurred at exactly those points. In other words, 9132 photons are emitted isotropically from each of these LUT and test points.

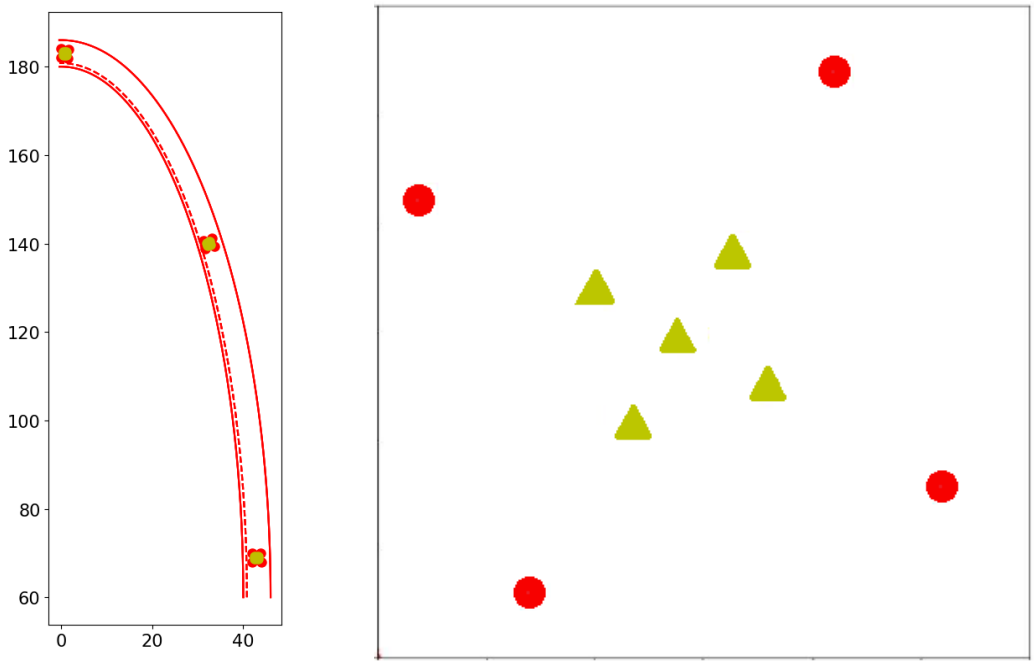

Figure 13. Regions and points chosen for simulation
Left: The three regions chosen (apex, central, base) are shown
Right: A zoomed-in image of the central region. Red circles represent points of the LUT (2mm apart). Yellow triangles are test points (2/3mm apart)

Since all of the points simulated so far were in a single slice of the crystal, we then used symmetry to justify rotation of the LUT points to form new LUT points. Each LUT point was rotated by 2mm about the central axis to obtain the remaining points that would make up the LUT. For each LUT point that was rotated, the scintillation photons that were simulated to have hit the outer surface of the crystal were also rotated by the same angle. The goal of this was to reduce unnecessary computation. By invoking rotational symmetry, the entire LUT can be generated by simulating a single central slice, and then rotating both the LUT points and their respective distributions along the outer surface of the crystal. When the points on the crystal's surface that represent the scintillation photons are rotated, the discretization algorithm is used to generate a new intensity distribution that is to be associated with the rotated LUT point.

3.3. Generation of Points for Developing LUT for Gamma Ray Simulation Verification

For the second set of simulations, gamma rays were used to test the localization algorithms and efficacy of the LUT as opposed to absorption events occurring at one point in space. This type of simulation is more realistic, as it accounts for the fact that the energy deposition of a gamma energizes an electron, which emits scintillation photons along some track as opposed to at exactly one point. Additionally, it accounts for energy deposition due to scatter of gamma rays (though the probability of scatter is quite low in this instance). Finally, with this set of simulations, the efficacy of the LUT can be observed along the entire depth of the crystal.

Though this simulation is more realistic, it is worth nothing that the CSDA range for an electron with 141keV of energy is about 0.1mm. With the maximum range being so low (and the average range of an electron produced by a gamma ray interaction even lower) relative to the 1mm distance of the LUT points (or 2mm distance in the previous set of simulations), the previous set of simulations is expected to be highly accurate.

To simulate the gamma rays, a location near the apex, central, and base region of the crystal, halfway into the crystal (i.e. 3mm in depth) was chosen. Recall that we justified simulating only a central slice or plane of the LUT, invoking rotational symmetry for generating the rest of the points, noting that the rotated points would also have a distance of ~1mm from the points they were rotated from. Thus, to make sure that the LUT and localization worked in 3D, we decided to shoot the gamma rays between the rotated set of points and original set of points, in each region. Effectively, the points chosen to send the gamma ray through were (0.65, 0.5, 122.98) at the apex, (37.45, 0.5, 60.0) in the central

region, and (42.0, 0.5, 3.25) at the base. (The 0.5 in the Y-direction is the aforementioned center of the rotated set of points and original set of points.).

After choosing this central point through which to send the gamma rays, 1000 gamma rays were sent in each direction, although ~1% of the gamma rays did not interact inside the crystal. Recall that originally, the LUT points that were to be simulated, if we were to generate the entire LUT, would've been 1mm apart. The LUT points in the vicinity of each of the gamma rays were also simulated to generate the new LUT. Figure 14 shows the line of sight of the gamma rays through each of the regions. ___ shows a zoomed-in view of each of the three regions and the limited number of nearby LUT points simulated (out of the total set of points).

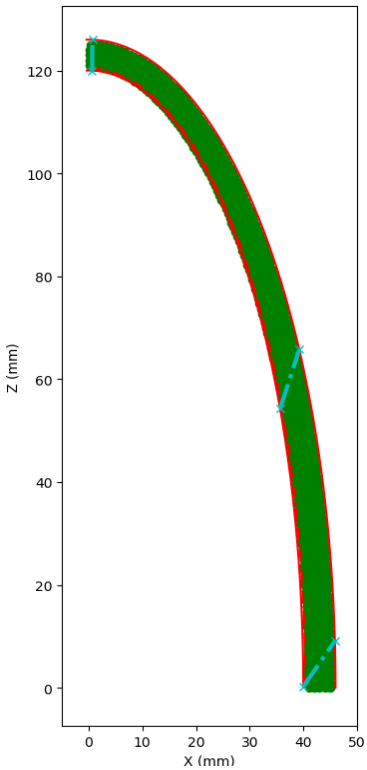

Figure 14. Path of gamma rays through crystal
The regions through which the gamma rays were sent is shown with the paths marked as a cyan line.

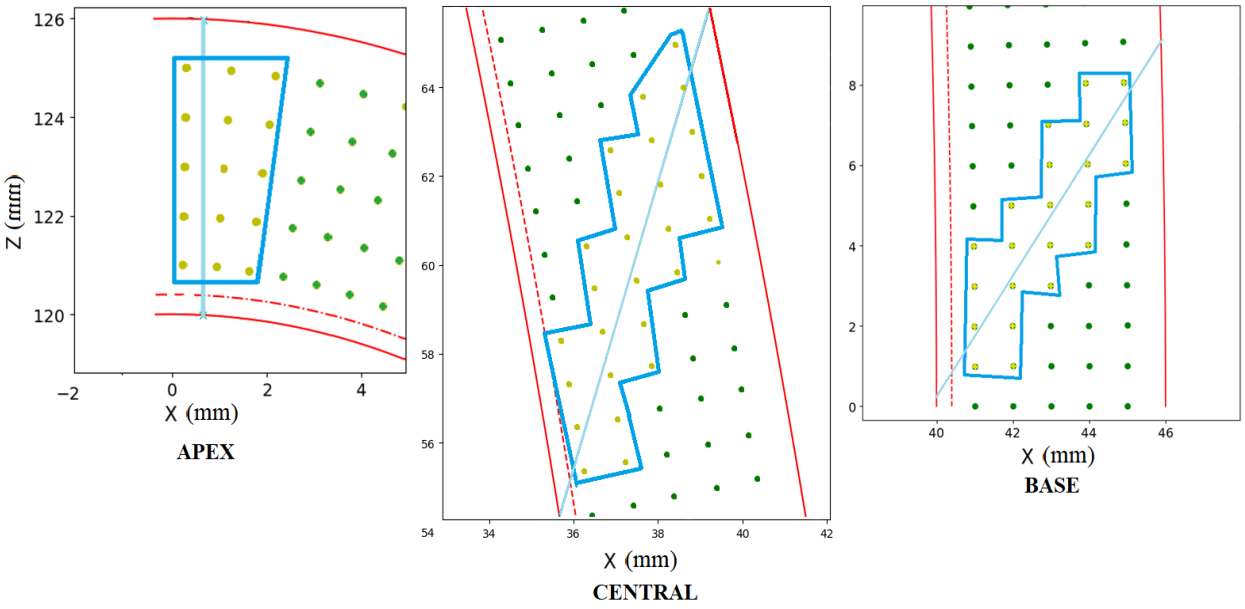

Figure 15. LUT points simulated near gamma ray paths

The regions through which the gamma rays were sent is shown with the paths marked as a cyan line. The dots represent all of the LUT points (zoomed-in), with the yellow dots in the blue polygon representing the LUT points chosen for simulation

Chapter 4. Aim 2: Localization Algorithms

This chapter details the steps taken to achieve localization. It includes discretization of the data obtained from the Geant4 Simulations (section 4.1), followed by the process taken to visualize, in 2D, intensities on a 3D surface (4.2). Subsequently, a discussion on a "region algorithm" follows which details how to statistically narrow down the search field (4.3), as well as implementation of the actual search algorithm and its improved variant (4.4).

4.1. Discretizing the Data

A method for creating physical bins to divide the data into segments is required. The bins should match, as closely as possible, real-life optical photosensors that will be added to the outer surface of the crystal during manufacturing. The bins should be small enough so that there is enough difference to be able to distinguish the intensity distributions of two nearby LUT points, yet not too small to make computation infeasible for millions of events. For the purposes of this study, we assumed 2mm by 2mm photosensors, such as APDs, would be placed around the outer surface of the crystal.

To discretize the data, we take note that the APDs are 2mm high. Thus, "rings", as shown in Figure 16, centered around the central axis of the ellipsoid were formed that were 2 mm high sections of the ellipsoid. For each ring, the radius of the lower circle was obtained via Equation 4.1 below (with a_o and c_o denoting the principal semi-axes of the outer crystal in the X and Y directions respectively) from the equation for an ellipsoid. By dividing a 2mm arc length by the radius obtained in the previous step, the angle dt_{exact} that would produce a sector on the outer surface of the crystal of exactly 2mm arc-length was calculated. An issue arises when we note that by having exactly 2mm arcs or bins on the

outer surface of the crystal, the "last" bin along an arc will never be exactly 2mm. That is, we can never evenly break up a ring into a whole number of arcs that are 2mm long (except in the theoretical and nonhelpful case where the radius is a multiple of $1/\pi$ and thus the circumference is an even whole number which can be divided into 2mm arcs completely). We take a few further steps to overcome this problem. We divide 2π by dt_{exact}, giving us the number of bins or arcs N_{exact} that would fully cover an entire ring. As this will always be a non-integer, we then round up the number of bins so that $N_{modified} = [[N_{exact}]]+1$. Then, we can obtain $dt_{modified}$ via $2\pi/N_{modified}$, where $dt_{modified}$ now is the angle (for that ring) that would cover the circumference of that ring with arcs that are just below 2mm long completely. Although it is un-realistic to have photosensors with such varied sizes in different rings of the crystal, if light guides are used, this is entirely possible. We've used this method so that bin-sizes are roughly equal, and no area of the crystal is left with a fraction of a bin.

$$r_{bottom} = \sqrt{\left(1 - \frac{y-2}{c_o^2}\right) a_o^2} \qquad (4.1)$$

This angle was used to calculate the approximate number of bins for each ring. It is valuable to note that as one traverses the ellipsoid from base to apex (the Y-direction), the shrinking sizes of the rings will result in a different number of bins (n_y) for each ring.

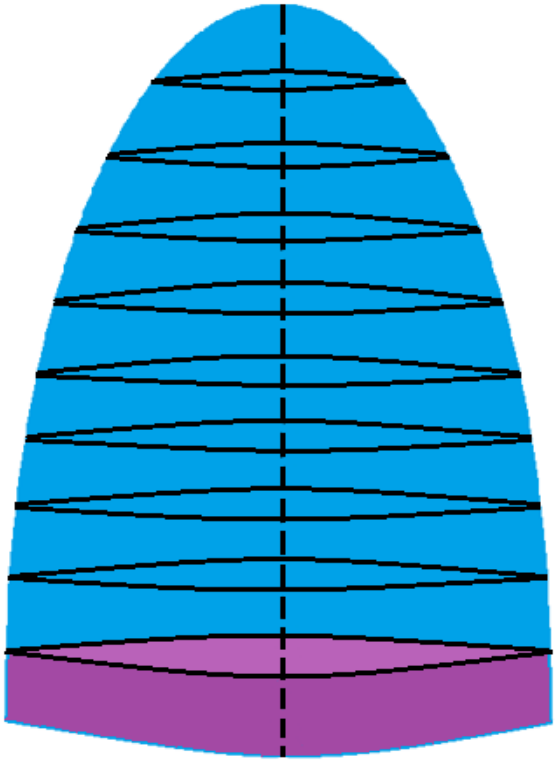

Figure 16. Visualization of rings used for discretization and binning
The ellipsoid is split into many rings 2mm in height (not shown to scale here) for the purposes of discretization and production of bins. The bottom ring is highlighted here.

At this point, we have broken up the entire outer surface of the crystal into rings, and broken each ring up into sectors that are 2mm high and have arc lengths slightly lower than 2mm. Now, we produce a way to refer to each of these bins so that counts can be accumulated in each bin and the data points can be discretized. We have chosen to refer to a particular bin with a key <Z, θ>. Z represents the height of the ring associated with that bin. Thus, with each ring being 2mm high, a point whose z-coordinate is 0.5 would fall in the first ring with Z=2, a point whose coordinate is 2.5 would fall in the second ring with Z=4, and a point whose coordinate is 4.0 would fall in the third ring with Z=6. θ represents the angle traversed from the point (0, r_{bottom}, Z-1) to get to the start of that bin. For example, for the first ring (at a height Z=2), $dt_{modified}$ is 0.04333 radians. Thus, the first bin

has a key <2,0>. The bin next to it, along the same ring, will have the key <2, 0.0433> and so on.

After the bins (specifically the bin keys) were created, the scintillation photons that were recorded from the Geant4 simulations were binned by matching their z-coordinate to the appropriate ring height and the x- and y-coordinates to the appropriate angle. For example, any point whose z-coordinate is in the range [0,2) and whose x- and y-coordinates form an angle in the range [0,0.04333) will have <2,0> as its key. If in a particular simulation there are 100 such points that meet these criteria, the counts accumulated for the <2,0> key will be recorded as 100. Thus, for each key, there is an associated count that is registered. For each LUT point, this is done for nearly 9,132,000 scintillation photons; recall that a mean number of 9,132 scintillation photons were generated from the absorption of 140.5keV gamma-rays and that 1000 such absorption events were simulated for each LUT point.

Figure 17 shows the binning procedure for some of the rings. As an example, the red star represents an incoming scintillation photon that hits the detector surface in Geant4. The binning algorithm would place the photon inside the yellow bin and increment the intensity of that bin by 1.

As a result of discretizing the data and accumulating the counts, a 1D output array of the counts or intensities was generated. This array will be referred to as BinCounts. Each row of this 2D array represents a ring in the discretization of the crystal, and each value in these rows or column represents the counts in each of the bins. As one travels toward the apex, the radius decreases, and thus the number of bins also decreases. Thus, the number of values in each subsequent row of BinCounts also decreases.

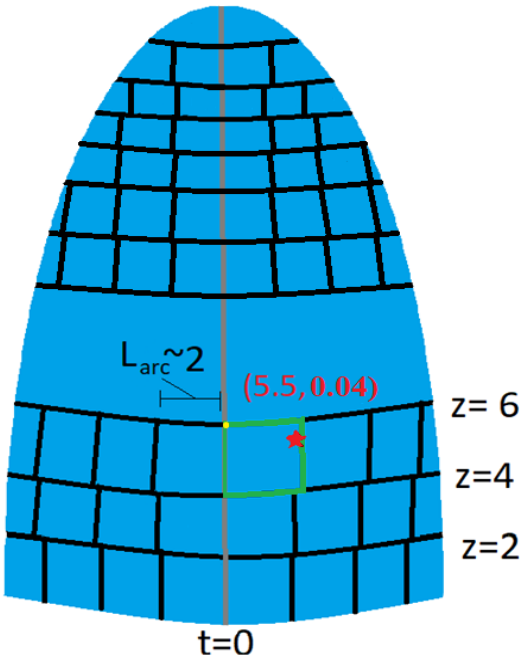

Figure 17. 2D Illustration of 3D bins

Each bin has a *key* <Z,θ>, where Z represents the height of the ring and the angle θ is determined by the x- and y-coordinates of the bin. The green-colored bin is represented by the key at the yellow point. An optical photon detected at the red star would result in an increment of the bin designated by that yellow key.

4.2. 2D Visualization of Intensities on Surface of 3D Ellipse

To visualize the intensity on the surface of the crystal, all that is needed is to slightly modify the BinCounts into a new array VA (short for Visualization Array). To do this, first BinCounts was transformed from a 1D to a 2Darray, with each row of the array representing bins in each ring of the crystal. Since the number of bins in each ring of the crystal, and thus each subsequent row of this new VisualizationArray, is less than the previous (due to the curvature of the crystal causing a decrease in the number of bins that go around a ring), the rows of VisualizationArray were padded with 0's so that each row became the same length. The padding was done on either side of the rows so as to center the data. Additionally, the array is flipped upside-down, so that the values at the top of the array (which represent the counts at the base of the crystal) then become at the top.

One way of understanding what this image represents is to imagine the ellipsoid being sliced along one side from base to apex and then unfolded open (like unrolling a toilet paper cylinder). The process described in this section is shown in Figure 18 for an arbitrary light distribution (of increasing intensity toward the apex direction).

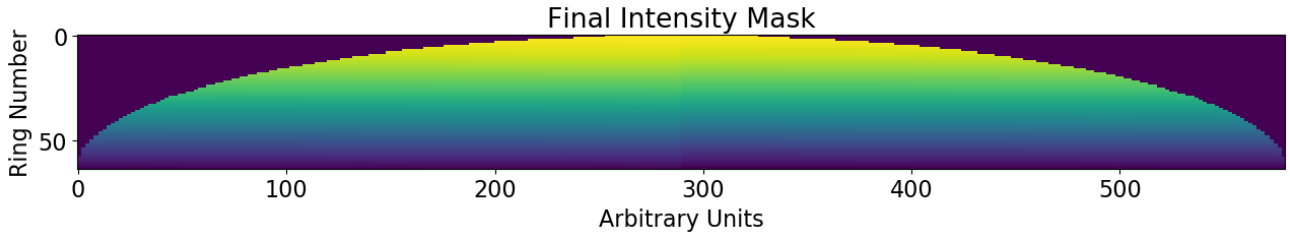

Figure 18. Visualization of 3D intensity distribution on a 2D image
A known-input of increasing intensity toward the apex was used to generate this visualization. (Intensities are uniform along each or row of the image—i.e. each ring of the crystal.)

4.3. Region Algorithm

For a new, incoming test point, it is inefficient to "search" and compare the distribution of the test point with the distribution of EVERY point of the LUT. In order to make the process computationally faster, it benefits us to greatly reduce the LUT points that need to be searched—to quickly localize the search area to a smaller region. We call this region localization algorithm our "region algorithm" as we narrow down the search area to within a small region or set of points. One method of narrowing down is geographical: find the bin with the maximum intensity, take some region near that bin of arbitrary radius, and search all LUT points in that region. Another option is that when a random scintillation event later occurs, we can take the bin with the highest intensity, and match it to the LUT point with the same highest-intensity bin—a one-to-one match. However, this can only be grossly correct due to random differences—that is, two different scintillation events (even at the same exact location) can generate distributions with

different maximum intensity bins. To avoid the arbitrary nature of the geometric method, and the inaccuracy of the single-bin matching, our implementation instead invokes Poisson statistics as explained below. Figure 19 illustrates our region algorithm procedure.

For all LUT points, the "mode-bin" (i.e., the bin with the most counts) was obtained. This bin will be referred to as <MB>. Its average is simply the counts in the modebin divided by 1000. The standard deviation of the counts in this mode bin across the 1000 runs is also calculated. (Recall that for each LUT point, 1000 runs were simulated. Each of these 1000 runs produces a different count in the modebin. The average number of counts and standard deviation of those counts is obtained from these 1000 runs.) It is noteworthy that the mean and standard deviation of the modebin for all of the LUT points very closely matched what was expected from Poisson statistics. (More on this in Chapter 5.1 Verification of Monte Carlo Simulation and Localization Algorithms.)

For now, let us call the average number of counts in <MB> MB_{avg} and the lower bound of this modebin, i.e. two standard deviations below this average, MB_{LB}. We now want to find all bins whose average counts are greater than MB_{LB}. We also want to find all of the bins whose upper bound is larger than the lower bound of the modebin MB_{LB} as well, where the upper bound of a bin is the average counts of that bin plus two standard deviations of that bin. Ideally, this would require us to calculate the standard deviation and mean of every single bin.

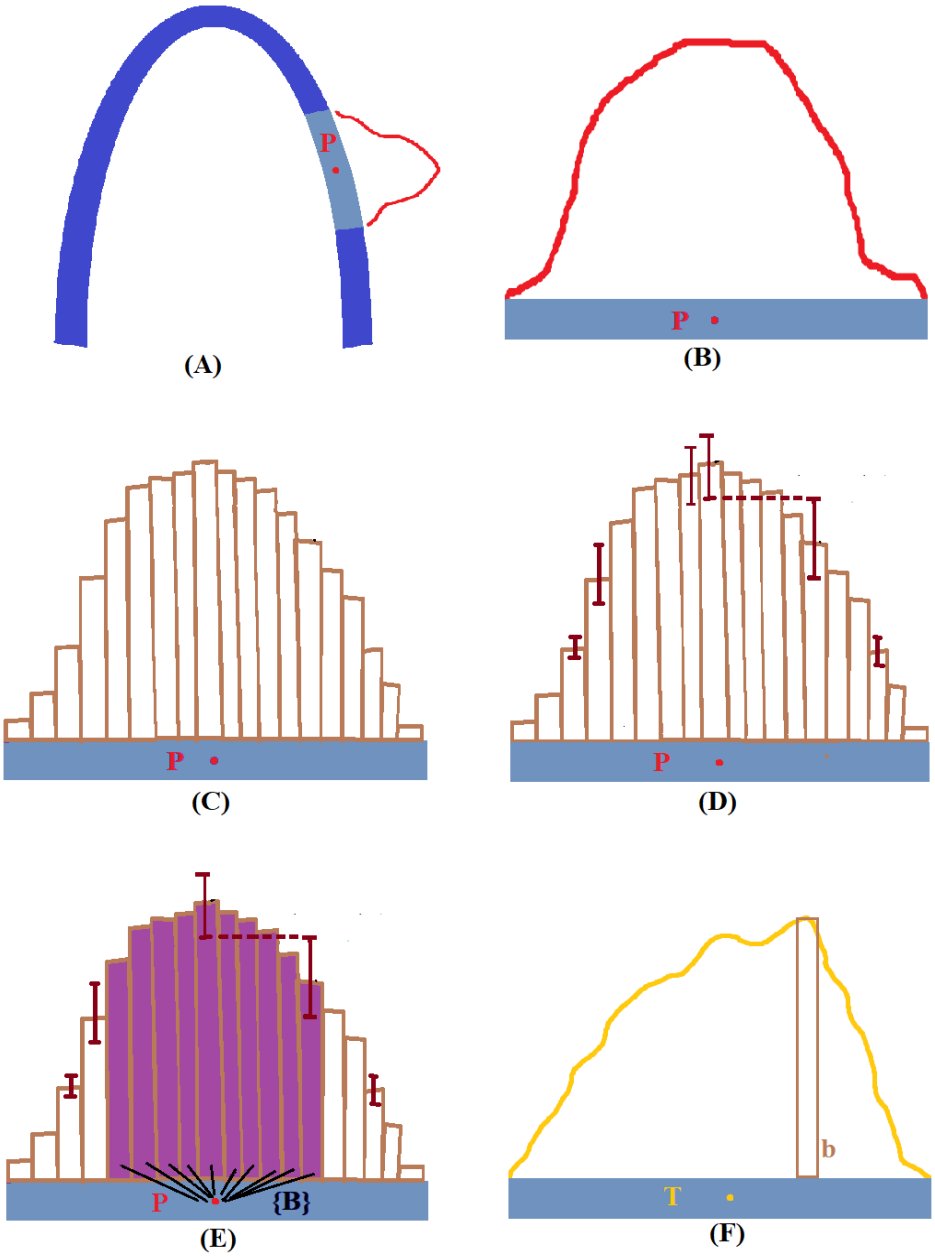

Figure 19. Step-by-step illustration of region algorithm

In (A), a point of the LUT, point P, is simulated with 1000 runs. For easier demonstration of the procedure, the segment of interest of the crystal is shown as a flat segment in (B). In (C), the data has been averaged and discretized into the appropriate bins. The average counts and standard deviation of some bins, including the modebin, is shown in (D). All bins {B} whose upper bound intersects the lower bound of the modebin are mapped to the point P as shown in (E). Later, when some incoming interaction occurs, even if it occurs at the same location as P, the resulting intensity distribution may be slightly dissimilar to the average expected distribution. However, as long as the modebin b for this incoming interaction falls within {B}, the point P will be considered for the matching algorithm.

We can circumvent this calculation by assuming Poisson statistics to be valid for all bins, or at least those bins with counts high enough to be near <MB>. (Note that we could also have invoked Poisson statistics for the modebin, but to be more accurate, we instead calculate the standard deviation of the modebin, unlike for the other bins.) Thus, we can instead set $MB_{LW} = c + 2s$, where c is the mean counts in a bin and s is the standard deviation of the counts in that bin. By invoking Poisson statistics, namely that $s = \sqrt{c}$, we can solve for c in the above equation to obtain $c = \left(1 - \sqrt{1 + MB_{LW}}\right)^2$, with c being the cutoff number of counts that a bin can have such that it is near enough the expected counts of <MB> that it needs to be considered when performing our localization algorithms. The following is an example scenario: Assume that the modebin had 400 counts on average and that its standard deviation was 20 exactly (perfect Poisson statistics). Thus, the lower bound for the modebin would be $400 - 2 \cdot 20$ or 360. Then, the upper bound of the cutoff bin would also have to be 360. This would make the number of counts which would be the cutoff c equal to 324, since the upper bound of a bin with a mean count of 324 would be given by $324 + 2 \cdot 18 = 360$. Thus, any bin that has a count of 324 or more would be included in the set of Bins $\{B\}_i$ associated with P_i. This example case is shown in Figure 20.

What we are essentially claiming by performing this procedure is that if a random scintillation event were to later occur at exactly one of the LUT point locations, through random chance, there is some probability that the maximum number of counts for that one event will not be in the expected <MB> but somewhere near <MB>. (Likewise, an interaction that doesn't occur at one of the LUT point locations but somewhere near it, through random chance, may produce its maximum number of counts in <MB>.) Thus, we create a mapping $P_i \rightarrow \{B\}_i$ of LUT points P_i to the set of bins $\{B\}_i$ whose upper bound counts

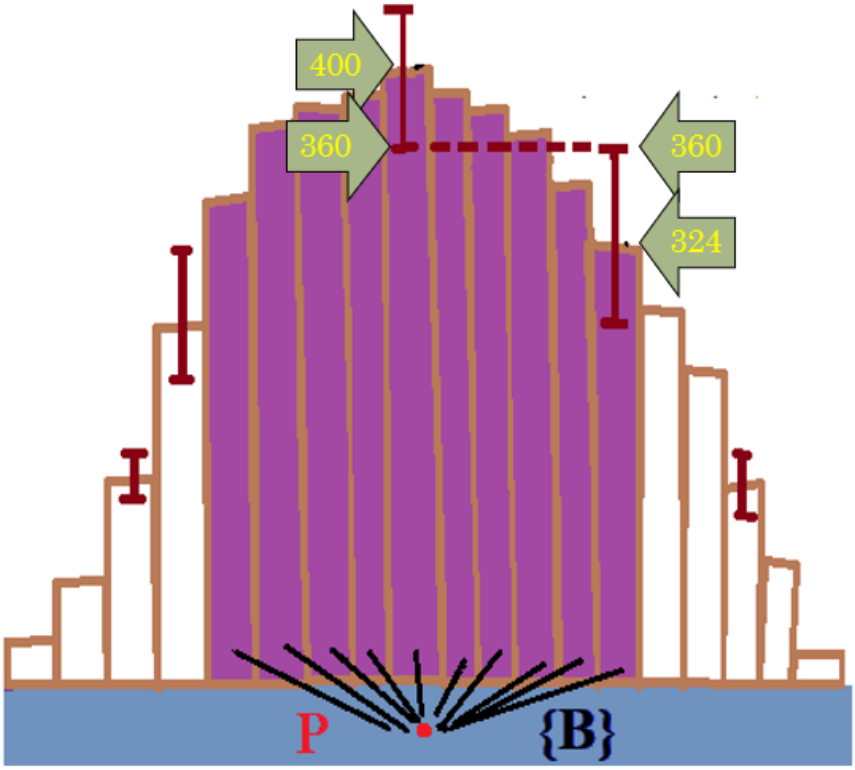

Figure 20. Example of region algorithm
By knowing the average number of counts and the standard deviation in the modebin, we can use Poisson statistics to calculate which bins would have an upper bound that would be within two standard deviations of the average in the modebin. Thus, with each LUT point P, a small set of bins {B} is associated.

fall within the lower bound counts of the modebin of P_i. Then, when a future random event occurs, it will produce its own maximum number of counts in some bin b. For all sets of $\{B\}_i$ that b is found to be in, the corresponding points P_i will be included in the localization algorithms discussed in the next section.

Assume now that an incoming gamma ray interacts exactly at one of the LUT points P, but that the bin with the highest number of counts generated by the scintillation does not coincide with the modebin of P, but actually with the modebin of some other LUT point, perhaps even the "next bin over". By implementing this region algorithm, we have included this "next bin over" in the set of bins $\{B\}$ which is associated with P. Thus, the point P is

included as a contender in the match algorithms discussed in the next section. Through this method, we are at least 95% confident that all the points considered for the matching algorithm includes the best matching point. Figure 19 shows a step-by-step demonstration of this procedure for further elucidation.

Because the random nature of incoming gamma rays may produce light distributions whose modebins do not result in any point being carried over to the matching algorithm, a safety mechanism was implemented. If the region algorithm cannot produce any points to search, then the modebin of the incoming gamma ray is used. The location of that modebin on the surface of the crystal is obtained and traced to a depth of 3mm normal to the surface, halfway into the crystal. Around this point, all LUT points within 5mm are carried forward to be used in the matching algorithm.

4.4. Match and Interpolation Algorithms

We employed a sum-squared error (SSE) match to compare the light distribution of those LUT points obtained from the previous step with the light distribution of the incoming test sources. The “match” algorithm simply calculates a bin-to-bin SSE and pins the test point as having occurred at the same location as the LUT point with the best match (lowest SSE). The interpolation algorithm goes a bit further. It performs an SSE-weighted interpolation by using the inverse of the eight smallest SSEs. The smaller the SSE, the larger its coordinates are weighted for determining the coordinates of the test point. This is illustrated with an example in Figure 21.

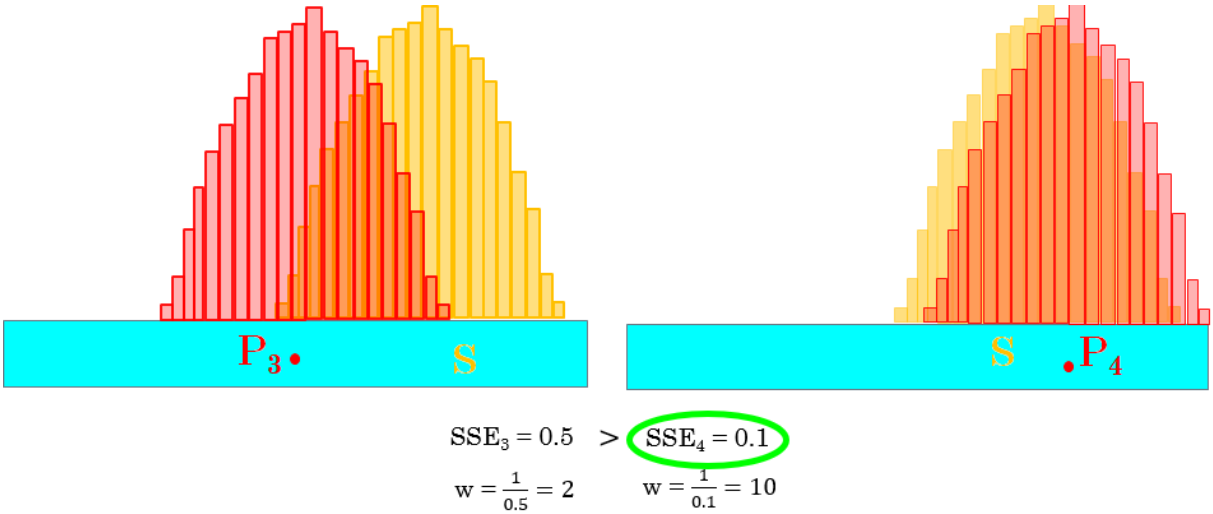

Figure 21. Example of match and interpolation algorithms

The figure shows the comparison of two LUT points (P3 and P4) with their light patterns in orange and an experimental point in yellow (S) with its light pattern in yellow. A bin-by-bin SSE is calculated for each match. Since the light pattern with P4 is the best match to the experimental light pattern, it has a lower SSE and a higher weight in interpolation.

Chapter 5. Aim 3: Verification and Validation

Verification and validation steps taken throughout the research process include verification that the algorithms work as intended, that the procedures produce the intended results, and assessment of the results and evaluation of the hypothesis.

5.1. Verification of Monte Carlo Simulation and Localization Algorithms

Verification of the algorithms was performed in various steps. Here, detailed ways are provided aside from general debugging of the code. The following steps all were taken to ensure that at each step of the way, the algorithms were providing the desired output.

The visualization in OpenGL of the Geant4 code as well as Geant4's default detailed output was used to ensure that the reflection was working properly and was diffuse reflection and that photons would stop as intended once they hit the photosensor (detecting) surface. Furthermore, known trajectories were given to photons and the photons were observed in OpenGL as well as the Geant4 default output and made sure to be hitting (and stopping at) the expected locations based on those trajectories. As the energy distribution needs to be provided as manual input for Geant4, this input was tested by generating then instantaneously terminating 100,000 scintillation photons and plotting the obtained energies of those photons to make sure that Geant4 was generating them based on the given distribution. Figure 22 shows the output of Geant4 compared to the input energy distribution. Notice that they are fairly similar although slightly varying in the central region (and agree statistically). Verification of Poisson statistics (and by extension, indirect verification of transport of photons), was also performed in two ways. Initially, it was performed by generating 1,000,000 scintillation photons at the location shown in Figure 23 and calculating the mean and standard deviation in a 1mm radius at the outer

surface of the crystal on the apex as shown. The mean from this procedure was 16.2 counts and the standard deviation was 15.4—a 5% difference in the expected value of the statistic. Secondarily, for the modebins obtained from the generated LUT points, Poisson statistics were verified as shown in Table 1. A maximum deviation from perfectly matching the expected Poisson statistic of about 10% difference was observed for the modebins of all 12 simulated LUT points.

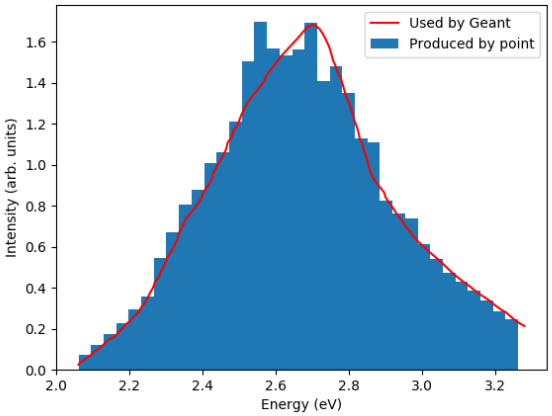

Figure 22. Verification of the energy distribution used by Geant4
The input energy distribution is given by the red line, whereas the output from Geant4 is given by the blue histogram.

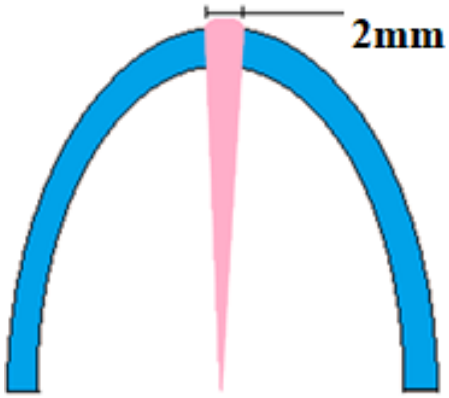

Figure 23. Procedure for verification of Poisson Statistics
The counts in the small region shown in pink were used to verify whether the output behaved as expected according to the Poisson distribution.

Table 1. Statistics for the modebin of the twelve LUT points

Region	LUT point	Mean	StdDev	Sqrt(Mean)	%Diff
Apex	A	97	10.75	9.85	8.37
Apex	B	120.4	11.8	10.97	7.03
Apex	C	136.7	12.9	11.69	9.38
Apex	D	259.7	16.6	16.12	2.89
Central	E	255.7	16	15.99	0.06
Central	F	247.3	15	15.73	-4.87
Central	G	487.8	21.3	22.09	-3.71
Central	H	452.9	19.9	21.28	-6.93
Base	I	225	14.2	15	-5.63
Base	J	227.5	14.4	15.08	-4.72
Base	K	440.8	19.8	21	-6.06
Base	L	444.11	20	21.07	-5.35

For verification of the binning algorithm, calculations were performed by hand and using Microsoft Excel for various rings and keys and compared to keys generated by the code. These were found to be matching. This not only validated the algorithm, but ensured that the equations used in the code were the proper equations to be used (such as the equation of an ellipse, etc.). Correct “snapping” of points to keys was checked by comparing by-hand calculations to those generated by the code. Known input data was also fed in to the binning algorithm to see if it would accumulate the counts in the bin correctly, which it did.

2D visualization was verified in a similar way: generated input data was fed into the algorithm (in the form of increasing intensity along a row, along the central column, and

along the rings, the last of which was shown previously in Figure 18). The resulting images were observed to ensure that the visualization matched the input data.

Verification of the region algorithm was again achieved through known input data that was manually generated. A Blank BinCounts was taken and certain entries were generated to become the modebin, while other bins were given various chosen counts. The cutoff number of counts was calculated by hand, and it was made sure that the region algorithm worked by including only those bins with counts above the calculated amount. This procedure was completed multiple times to verify whether the algorithm was correctly picking out the points P_i for which an incoming gamma ray generated a modebin that fell within the points' associated set of bins $\{B\}_i$. In the next verification step, a snippet of code was written which checked to ensure that with a known input modebin b (such as would be generated by an incoming gamma ray), the algorithm would set aside for the match algorithm those points for which b was in $\{B\}_i$. The matching and interpolation algorithms were also checked using generated data. Firstly, a value of 0 was obtained as the SSE between two of the same matrices, as expected. On top of that, the calculated SSE for manually generated matrices matched the SSE given by the algorithm.

5.2. Primary Validation Using Test Points Generated via Simulation of Scintillation Photons

The figures below (Figure 24 through Figure 26) show a zoomed-in view of the intensity distributions of the twelve LUT points. The differences in their distributions are easily visible. Recall that these LUT points were arranged in a square-like shape with distances between adjacent LUT points of about 2mm.

The matching algorithm was performed on the 15 test points discussed in Section 3.2 for the three regions previously shown in Figure 13. Table 2 summarizes the results

(with test points that matched correctly shaded green and test points that matched incorrectly shaded red), and Figure 27 illustrates the results of the interpolation algorithm. Note that all test points in the base and middle regions of the crystal matched to the nearest LUT points. However, in the apex, this was not the case. All of the test points matched to the "bottom right" LUT point, showing an obvious bias in depth and away from the apex.

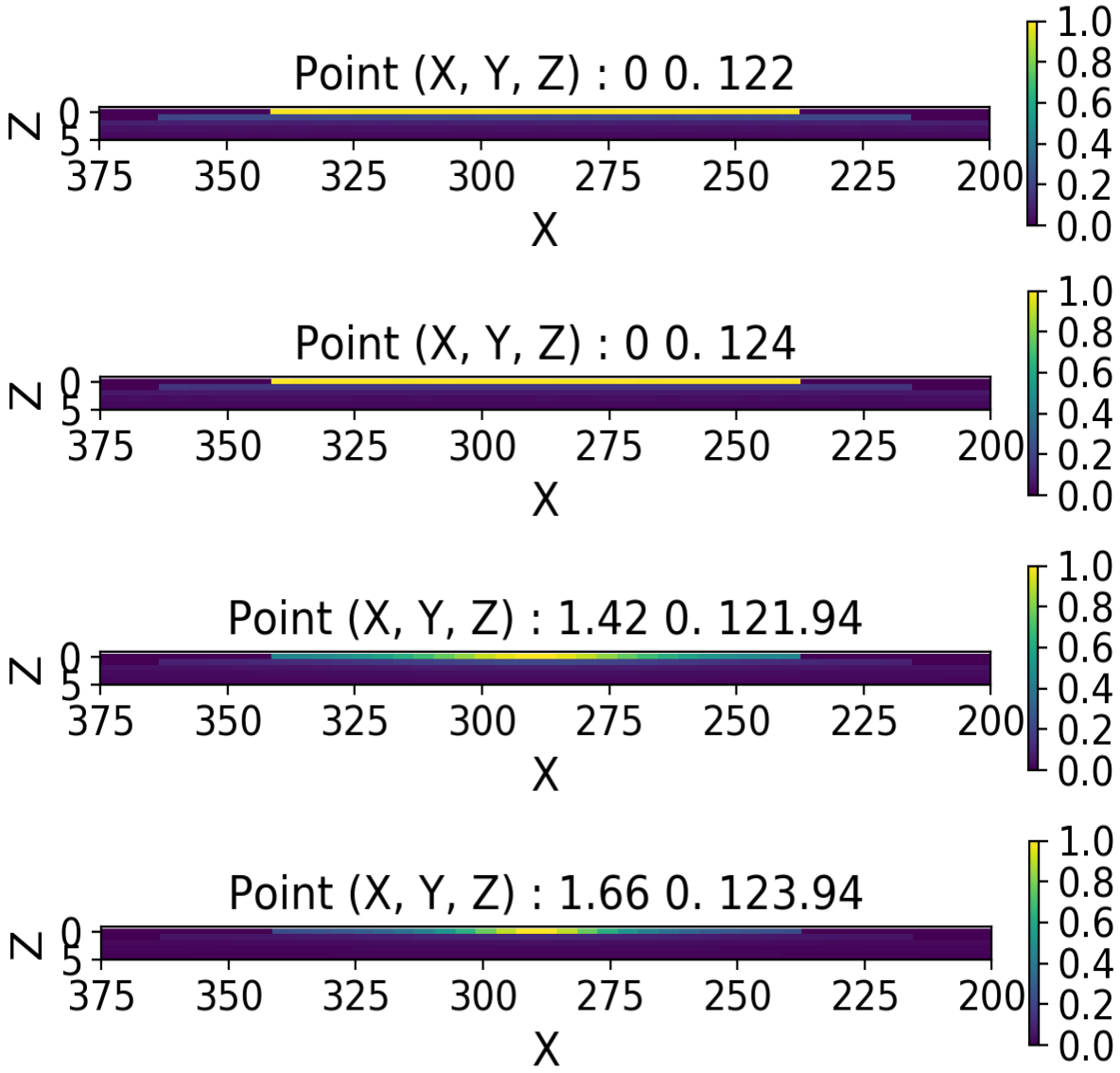

Figure 24. Light distribution of LUT points at apex
The light distribution of the four LUT points at the apex are shown. From top to bottom, they are the upper left, lower left, upper right, and lower right LUT points in that region.

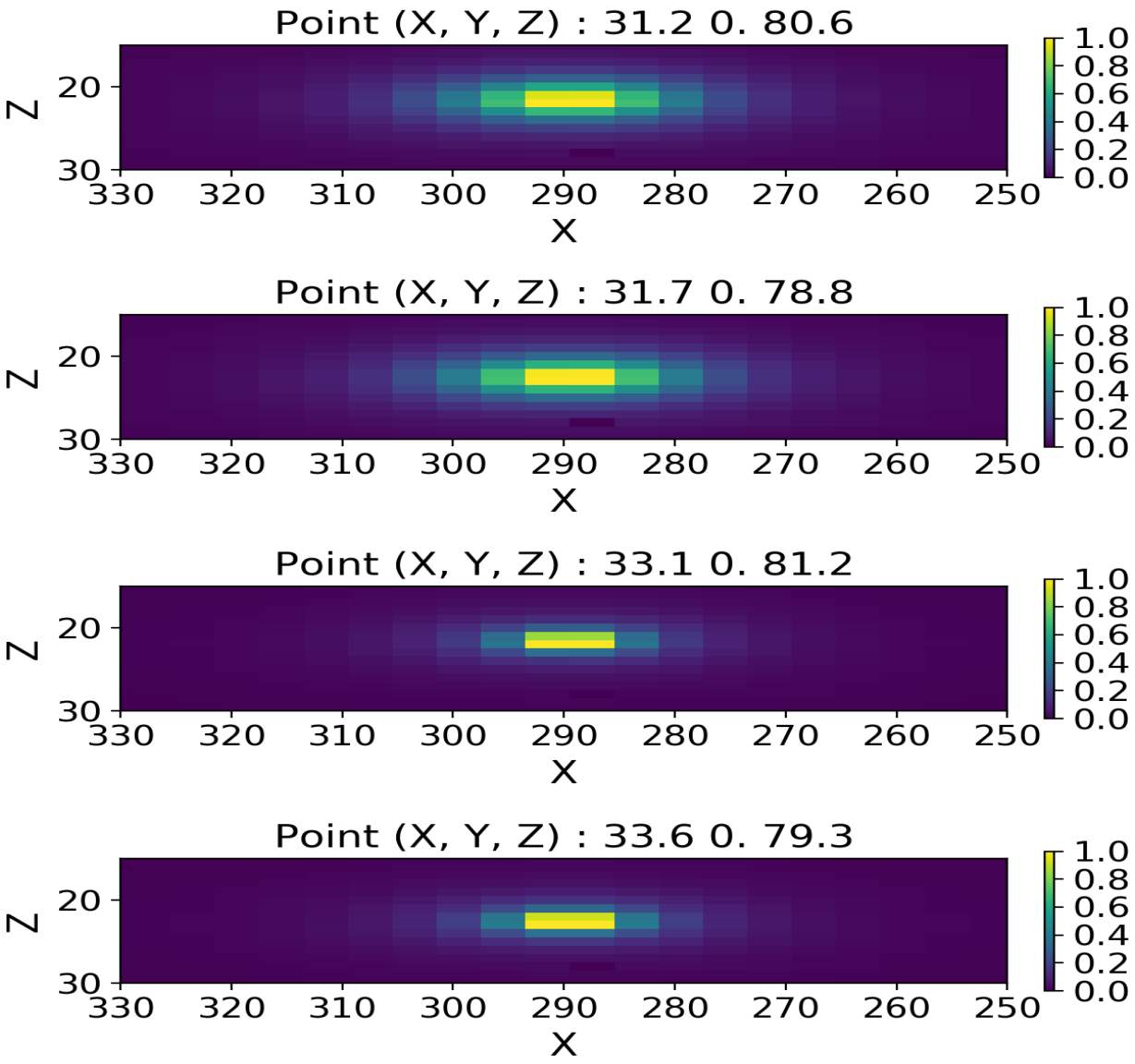

Figure 25. Light distribution of LUT points at the central region

The light distribution of the four LUT points at the central region are shown. From top to bottom, they are the upper left, lower left, upper right, and lower right LUT points in that region.

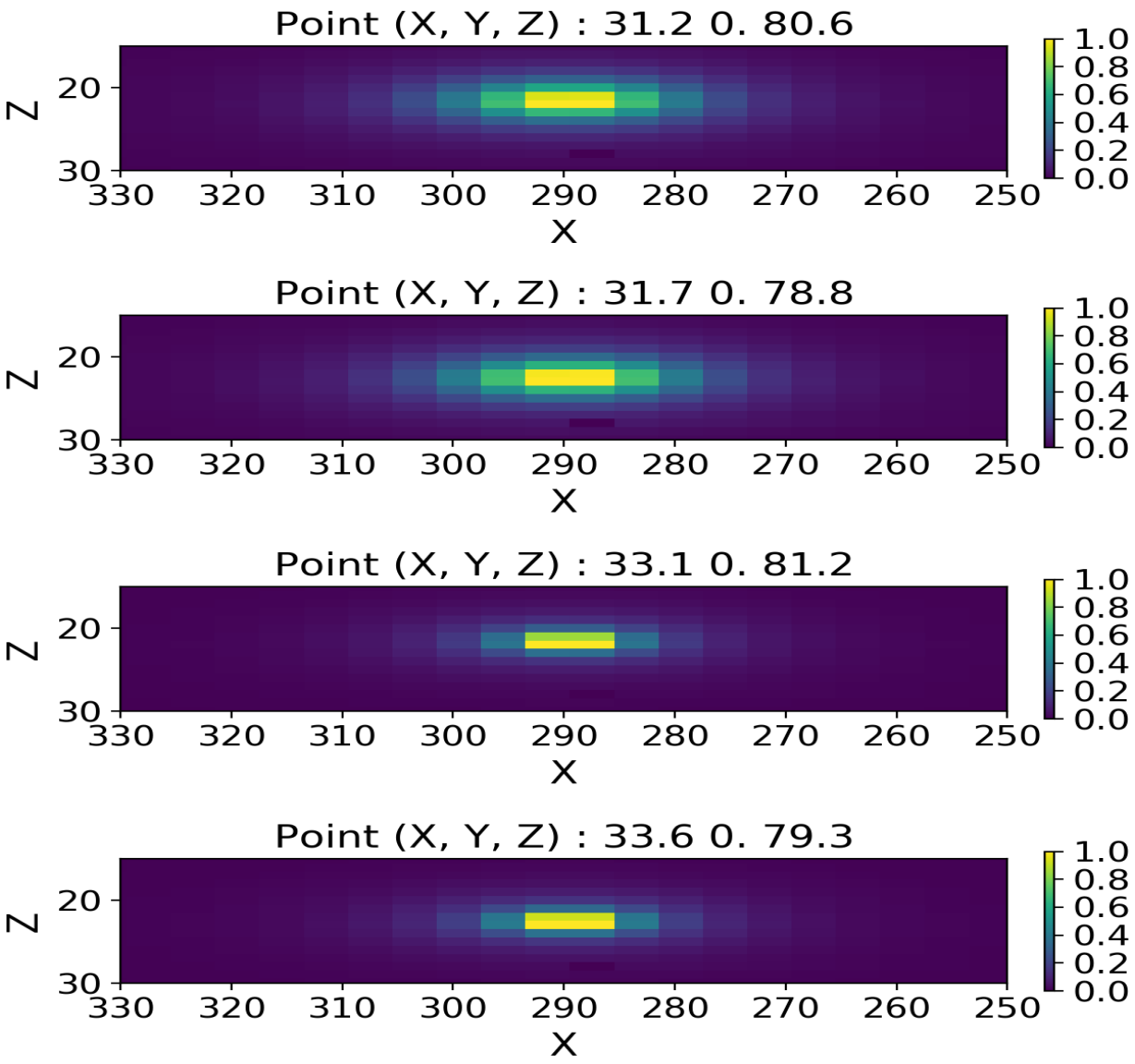

Figure 26. Light distribution of LUT points at base

The light distribution of the four LUT points at the base are shown. From top to bottom, they are the upper left, lower left, upper right, and lower right LUT points in that region.

Table 2. Results of Validation using test points generated as an absorption effect

Region	Test Point's Relative Location	Relative Location of LUT Point to which Test Point Matched	Closest LUT Point?	Distance (mm) Between Interpolated Point and Test Point
Base	Top Left	Top Left	Yes	0.073
Base	Bottom Left	Bottom Left	Yes	0.121
Base	Center	Bottom Right	--	0.18
Base	Top Right	Top Right	Yes	0.399
Base	Bottom Right	Bottom Right	Yes	0.437
Middle	Top Left	Top Left	Yes	0.05
Middle	Bottom Left	Bottom Left	Yes	0.078
Middle	Center	Bottom Right	--	0.067
Middle	Top Right	Top Right	Yes	0.149
Middle	Bottom Right	Bottom Right	Yes	0.114
Apex	Bottom Left	Bottom right	No	0.377
Apex	Top Left	Bottom right	No	0.544
Apex	Center	Bottom Right	--	1.218
Apex	Bottom Right	Bottom right	Yes	0.813
Apex	Top Right	Bottom right	No	1.395

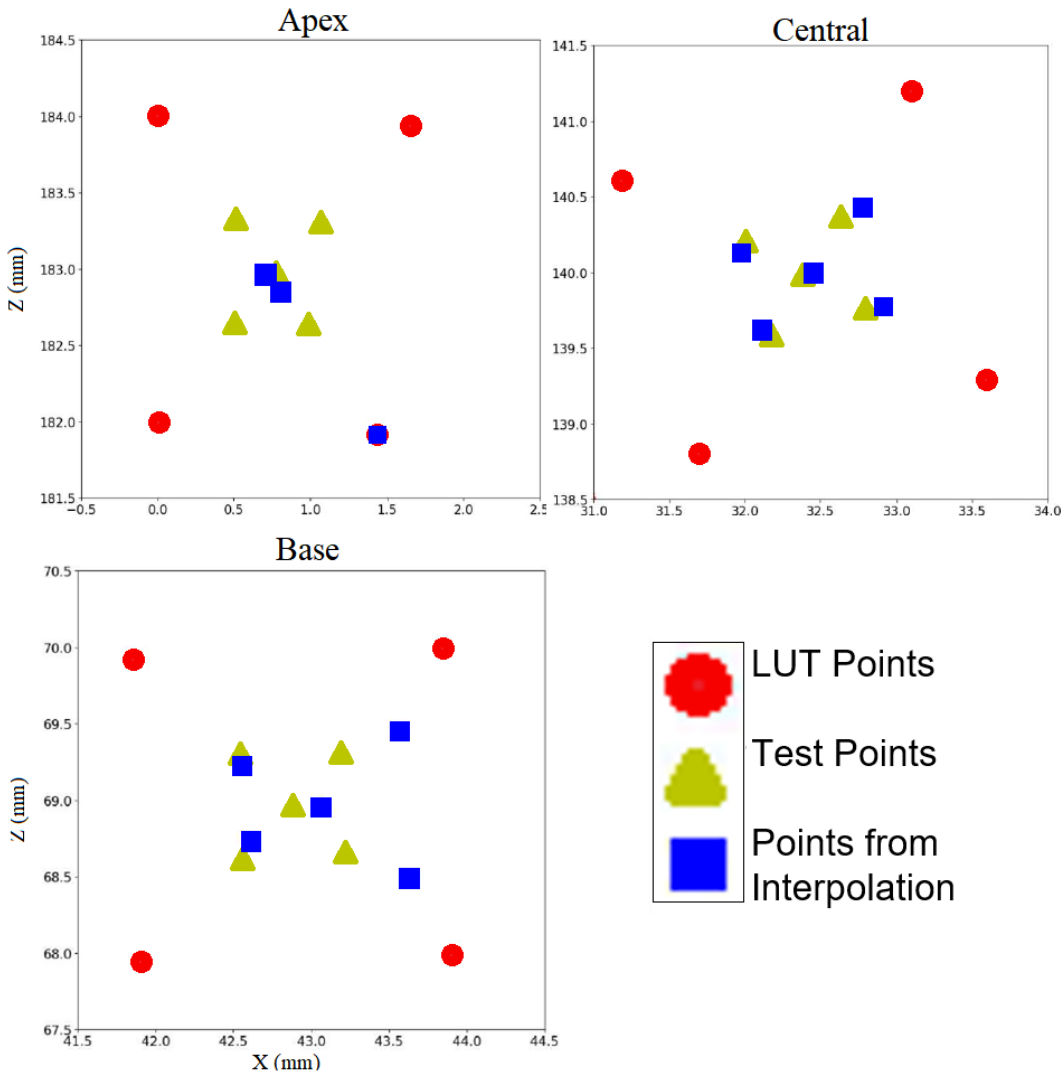

Figure 27. Results of Interpolation Algorithm
For the Apex (top left), Central (top right), and base (bottom left) regions of the crystal, the results of the interpolation algorithms are shown as blue squares. The yellow triangles are the locations of the original test points. Note that for the central and base regions, the deviation between the test points and interpolated localization is small. For the Apex region however, the interpolation algorithm localizes many of the points straight to the LUT point on the lower right.

5.3. In-depth Validation Using Gamma Rays

The gamma rays discussed in section 3.3 were simulated. The rotation algorithm was used to generate a new "plane" of points that were rotated by 1mm. (The rotated set of point do not lie on an exact plane—the radii of the rotation circles are not exactly the same, and so

the points do not end up lying on the same plane, but are roughly planar). The points are shown in various orientations in 3D as well as in 2D projections onto the XZ-plane for the three different regions in the following figures: Figure 32 through Figure 35 show the apex region, Figure 32 through Figure 35 show the central region, and Figure 36 through Figure 39 show the base region. In all of the figures, the red dots represent the first interaction point that produced scintillation photons (so if a Compton Scatter event occurred, not producing scintillation photons, and the scattered gamma ray traveled far away and then was absorbed causing a scintillation event, the location at which it was absorbed would be marked by a red dot). In all figures, yellow dots represent the LUT points. In some figures, a partial outline of the ellipsoid is shown for easier visualization/orientation in the 3D space. It is noteworthy that in all cases, there were points that interacted far away from the path of the gamma ray (due to Compton scatter interactions).

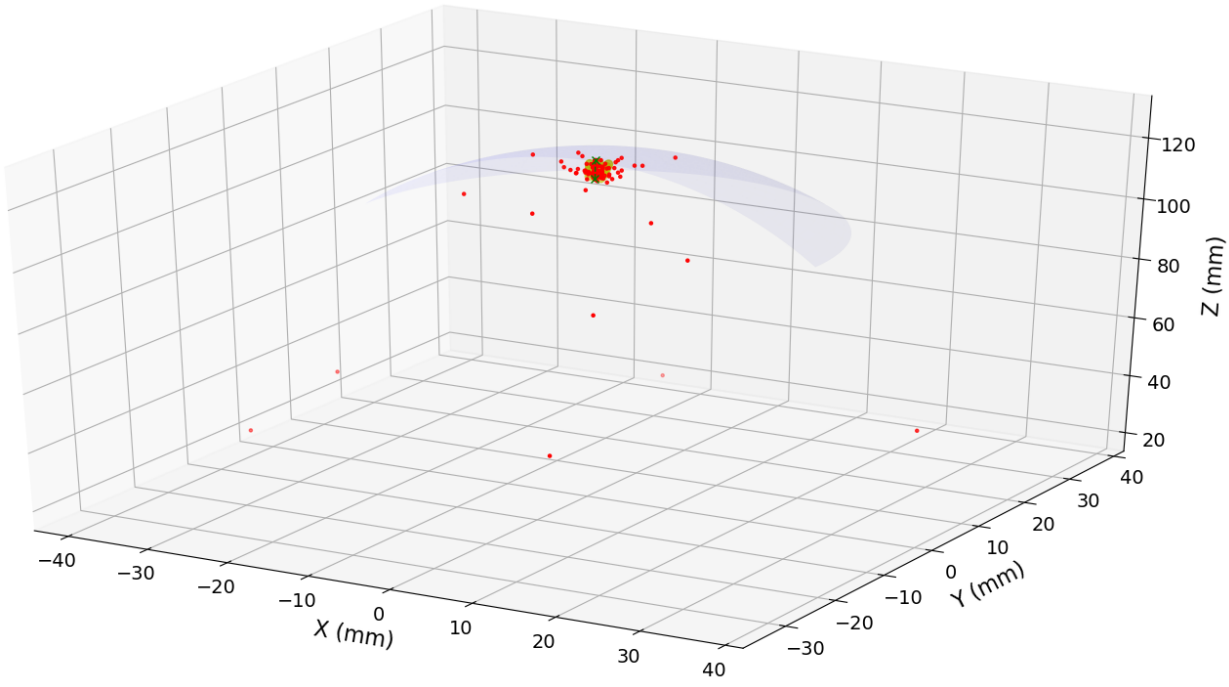

Figure 28. LUT points and gamma ray interactions at apex region in 3D

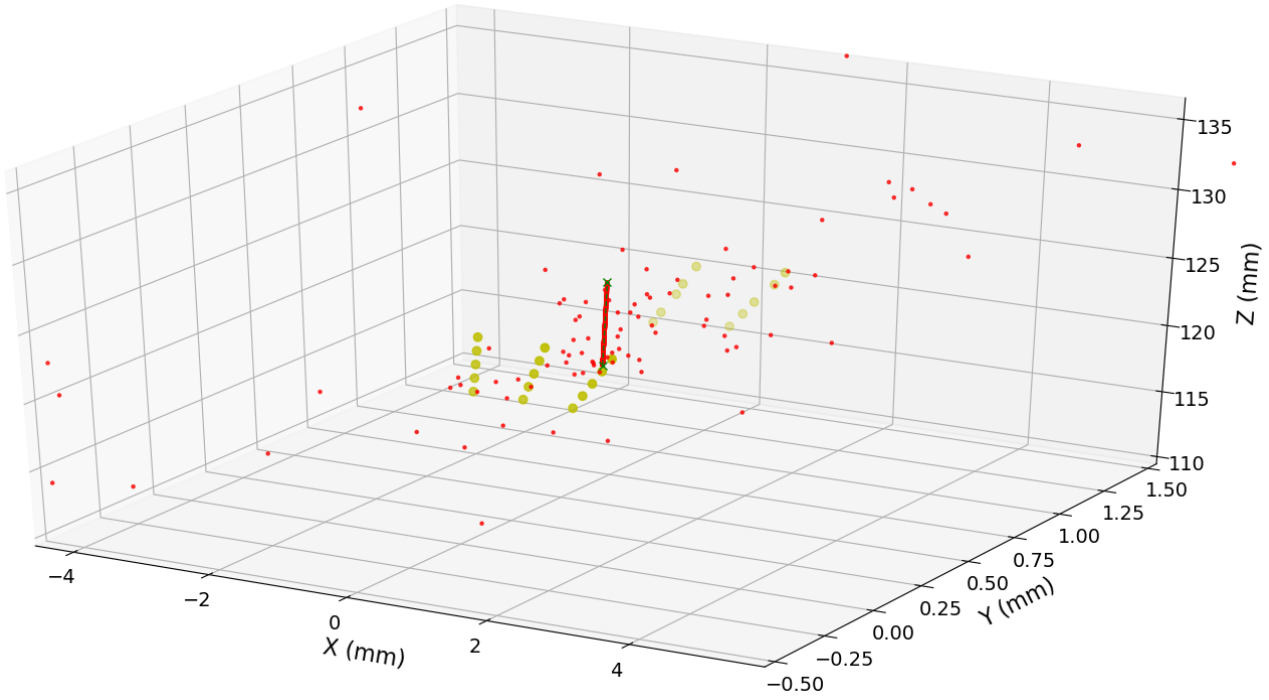

Figure 29. LUT points and gamma ray interactions at apex region—zoomed in 3D
Notice that we have included the rotated LUT points that were generated via the rotation algorithm.

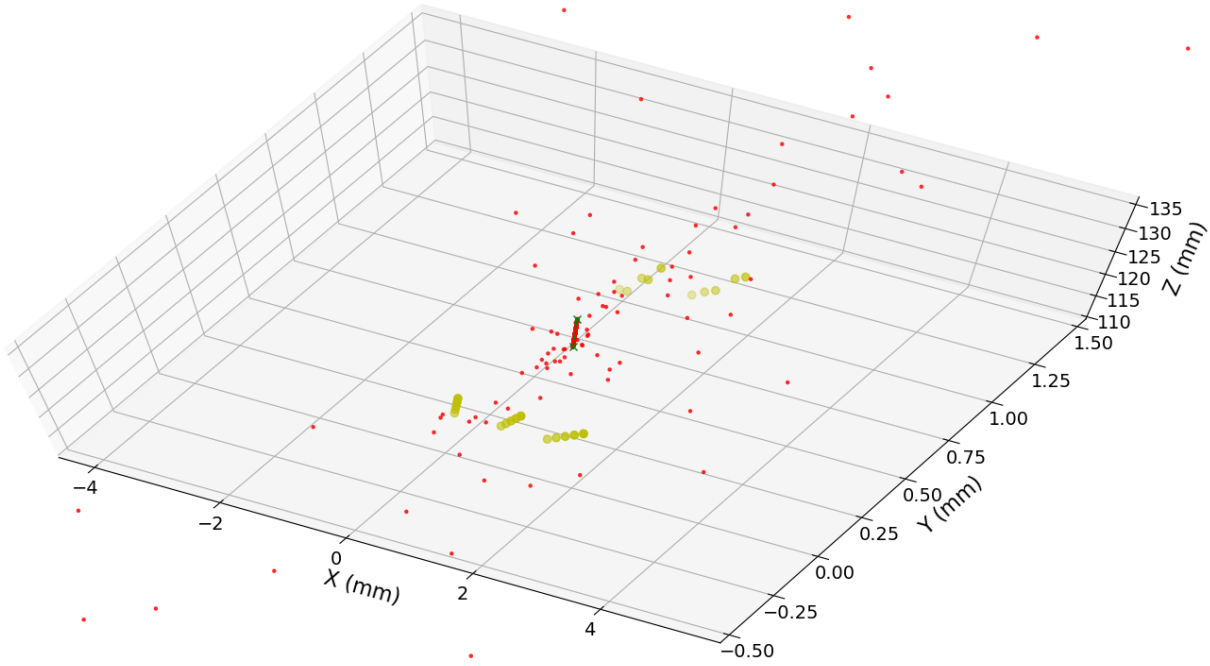

Figure 30. LUT points & gamma interactions at apex region—zoomed & rotated 3D
Notice how the gamma ray path is in the center of the two "planes' of LUT points.

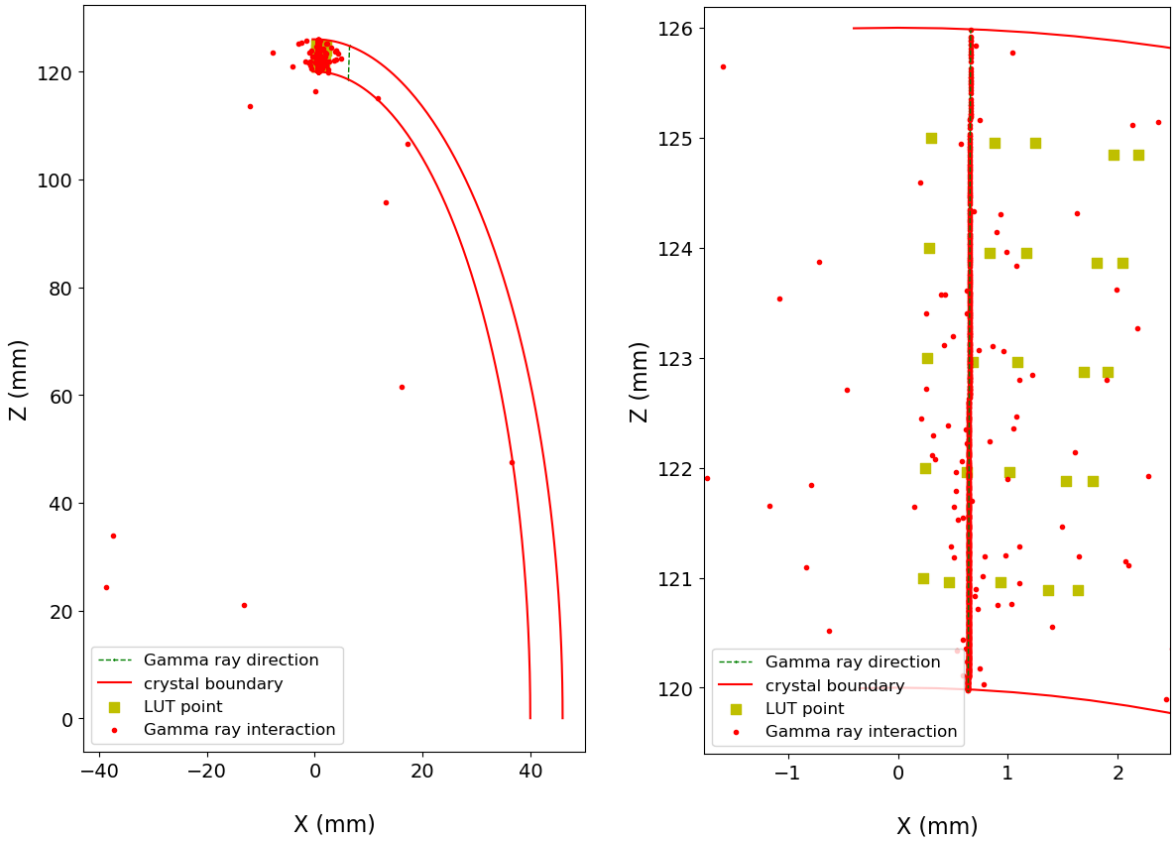

Figure 31. LUT points & gamma interactions at apex—2D projection onto XZ plane

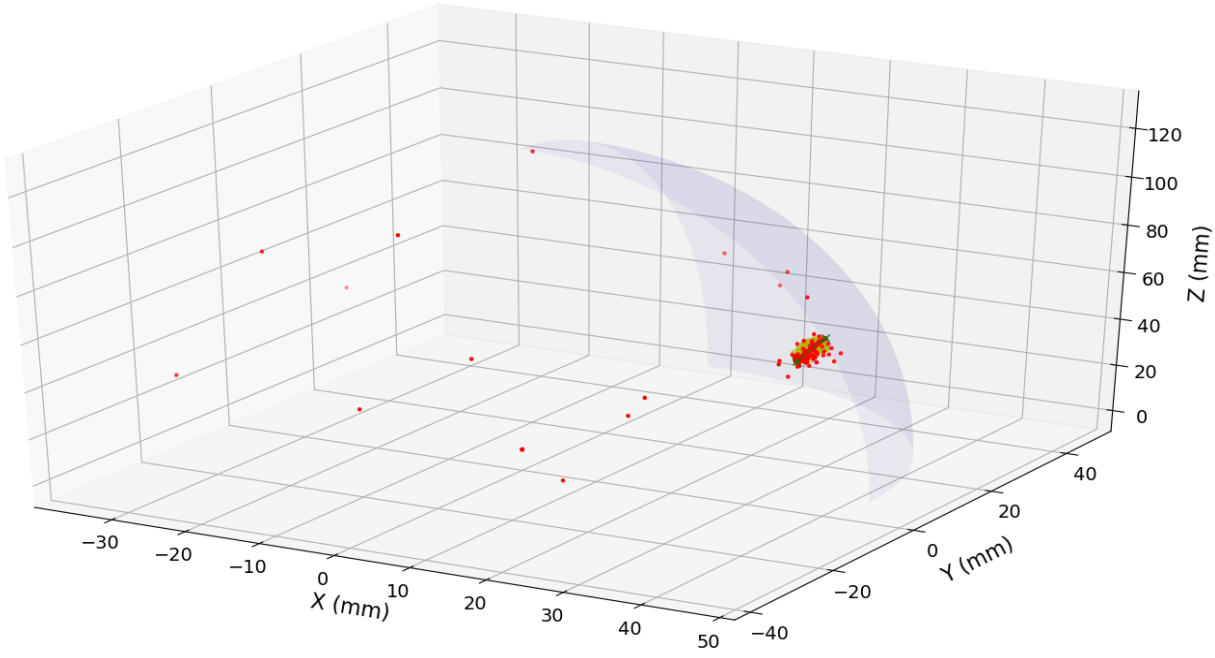

Figure 32. LUT points and gamma ray interactions at central region in 3D

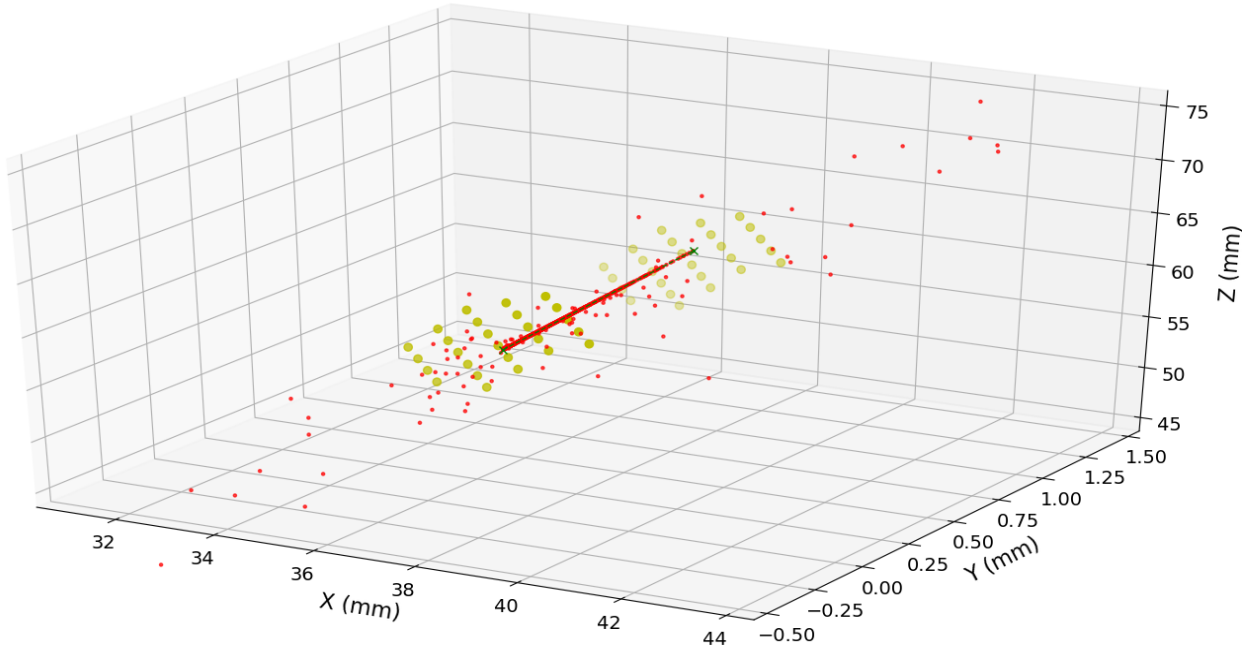

Figure 33. LUT points and gamma ray interactions at central region—zoomed in 3D
Notice that we have included the rotated LUT points that were generated via the rotation algorithm.

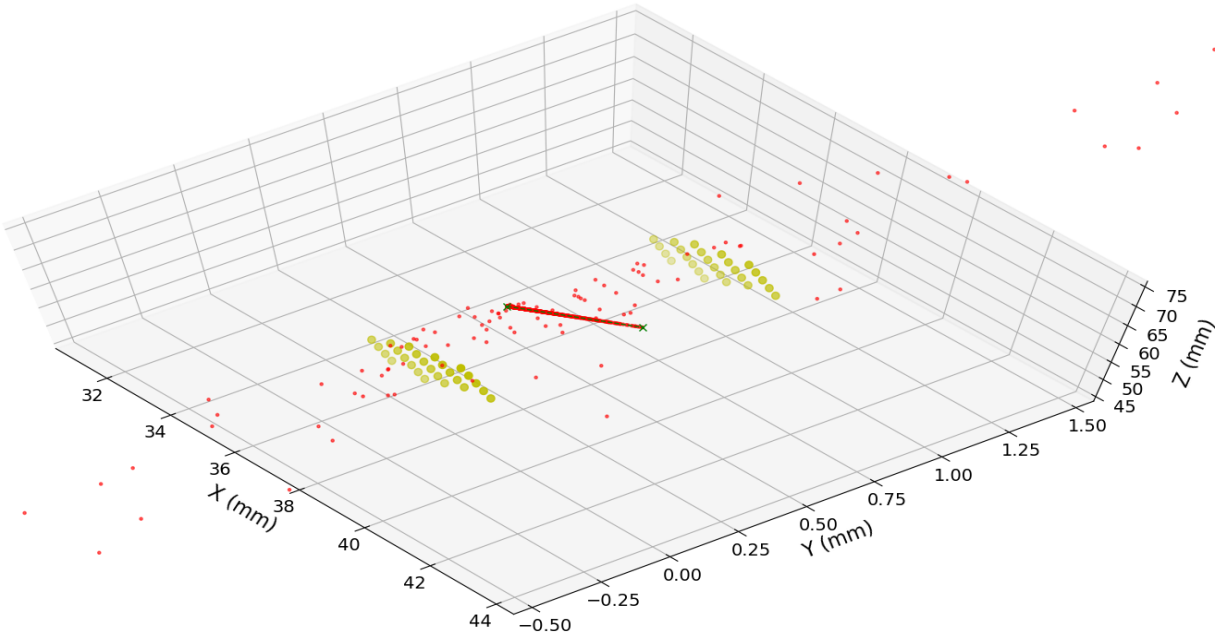

Figure 34. LUT points & gamma interactions at central region—zoomed & rotated 3D
Notice how the gamma ray path is in the center of the two "planes' of LUT points.

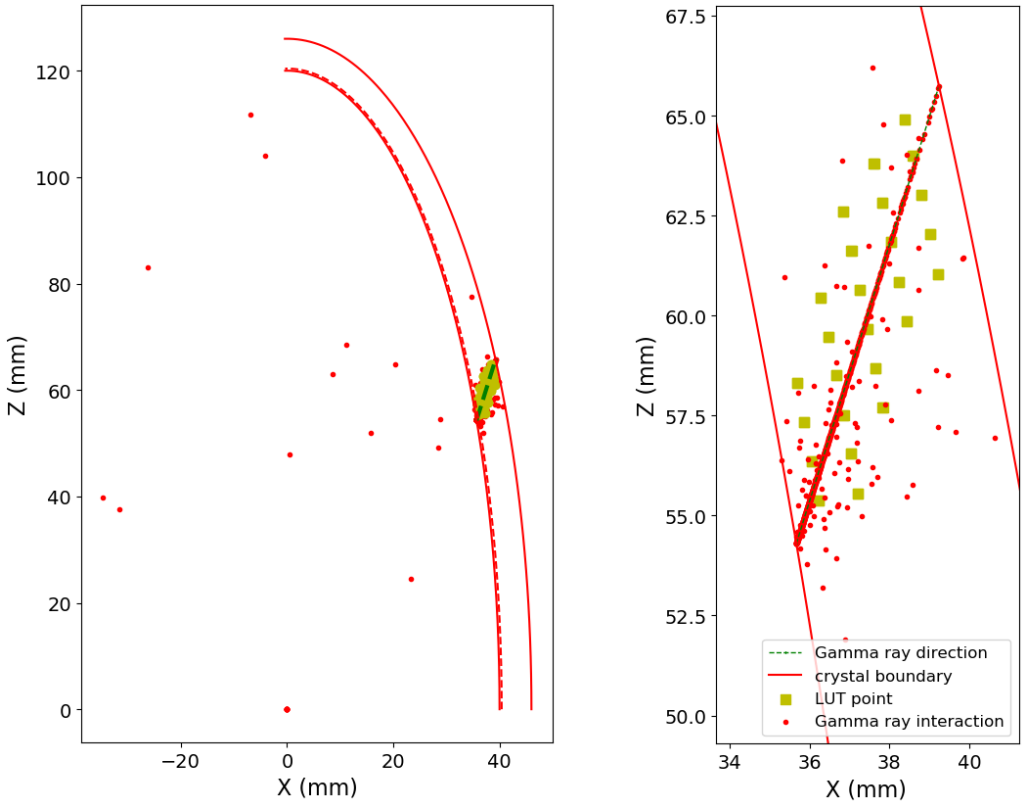

Figure 35. LUT points & gamma interactions at central region—2D projection onto XZ plane

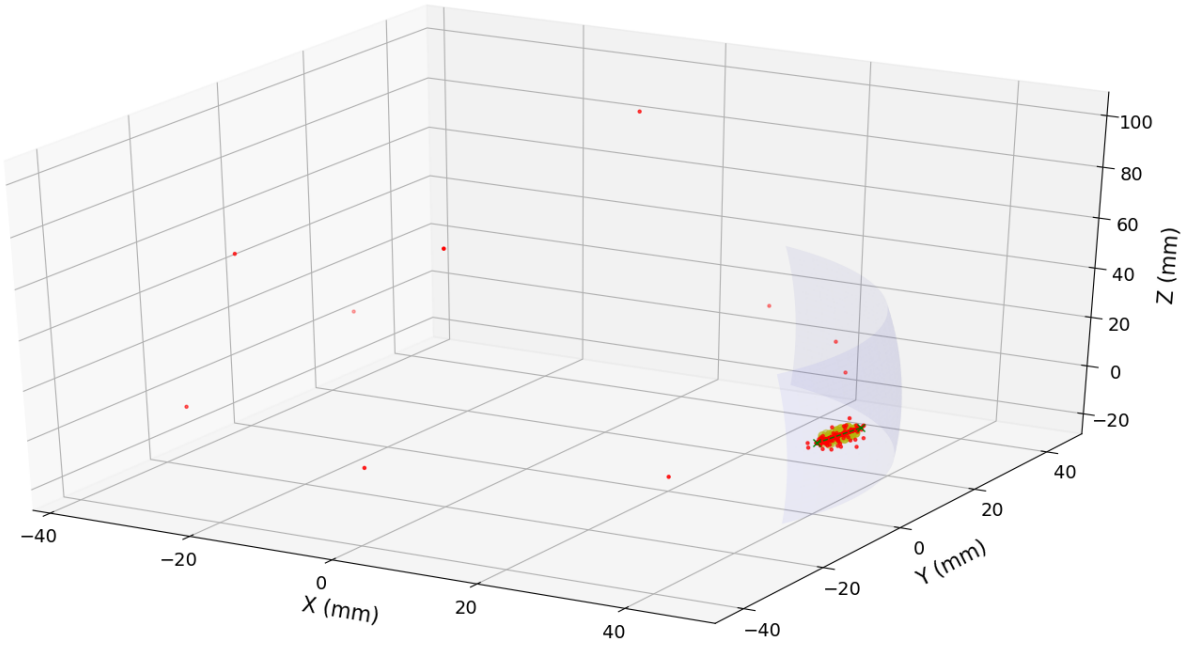

Figure 36. LUT points and gamma ray interactions at base region in 3D

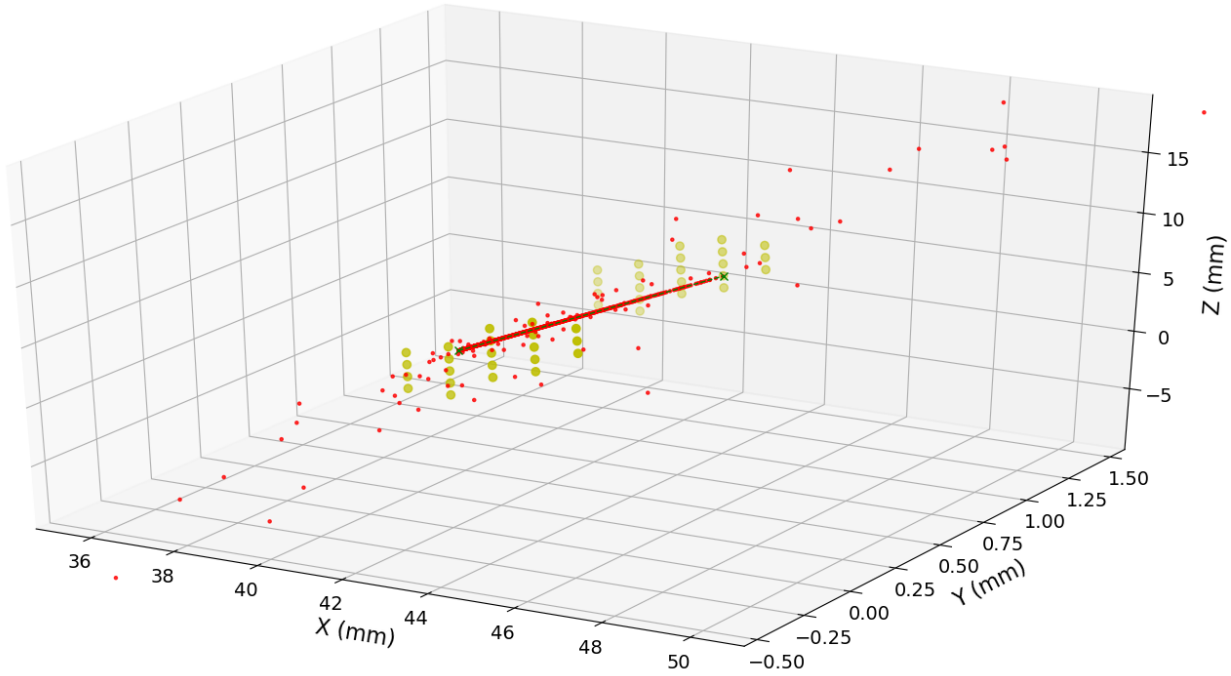

Figure 37. LUT points and gamma ray interactions at base region—zoomed in 3D
Notice that we have included the rotated LUT points that were generated via the rotation algorithm.

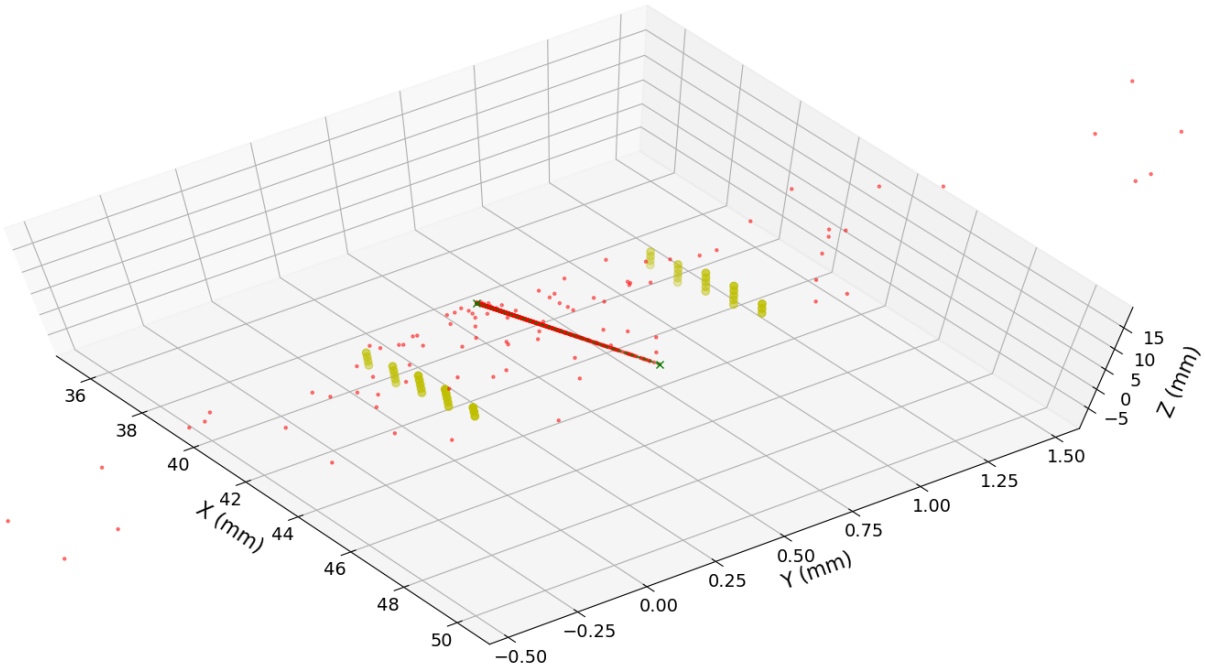

Figure 38. LUT points & gamma interactions at base region—zoomed & rotated 3D
Notice how the gamma ray path is in the center of the two "planes' of LUT points.

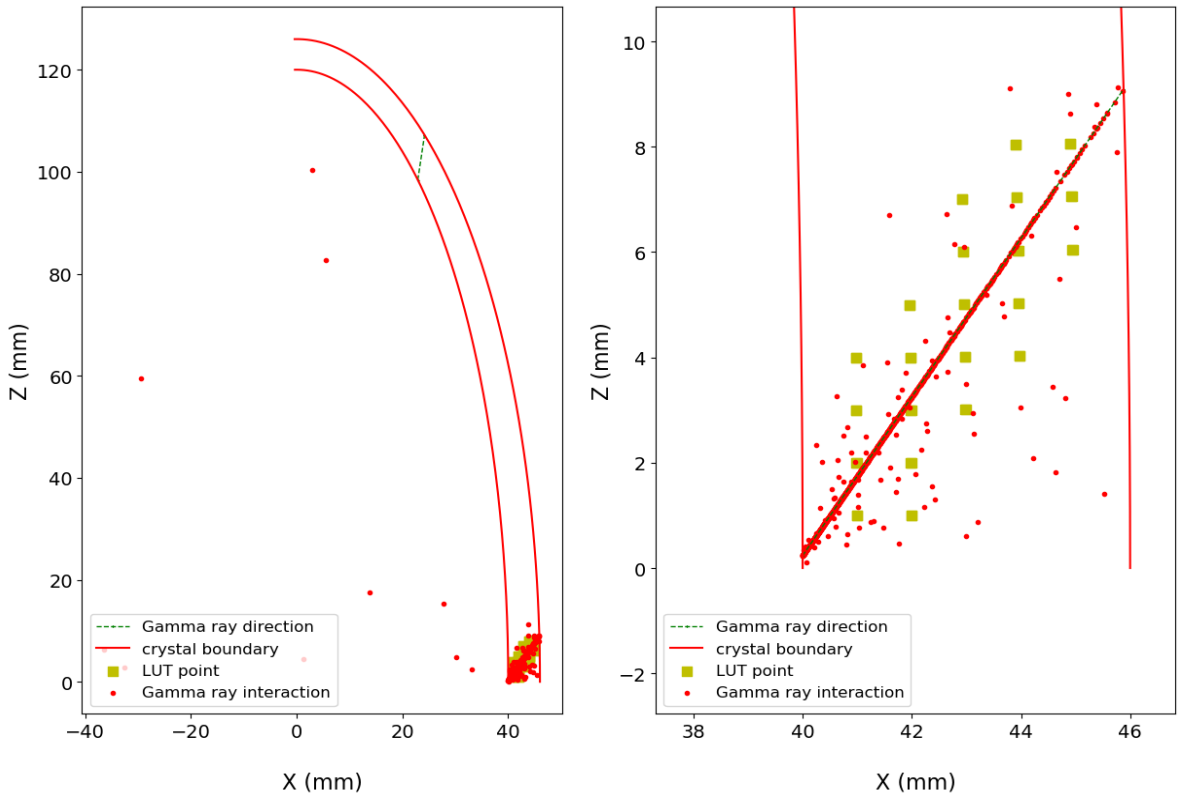

Figure 39. LUT points & gamma interactions at base region—2D projection onto XZ plane

The distances between the interactions and the nearest LUT point is shown in histograms for the three regions in Figure 40 through Figure 42. Table 3 summarizes these graphs in table form. Table 4 then gives information about how far each of the points were from the gamma ray's path. The majority of the gamma rays (87.4%—88.2%, depending on the region) interacted along the initial path of the gamma ray without Compton scattering. Some rays (8.9%—9.4%) Compton-scattered very closely (within 2mm) to the initial gamma ray path, and a small percentage of rays (2.8%—3.7%) ended up interacting far away (greater than 2mm) from the path of the gamma ray. having first interacted via a Compton scatter event and travelled far from the path of the initial gamma ray. These points that scattered far away, which are statistical outliers, were not included in the interpolation algorithm, as there was no generated LUT points in the regions they scattered to.

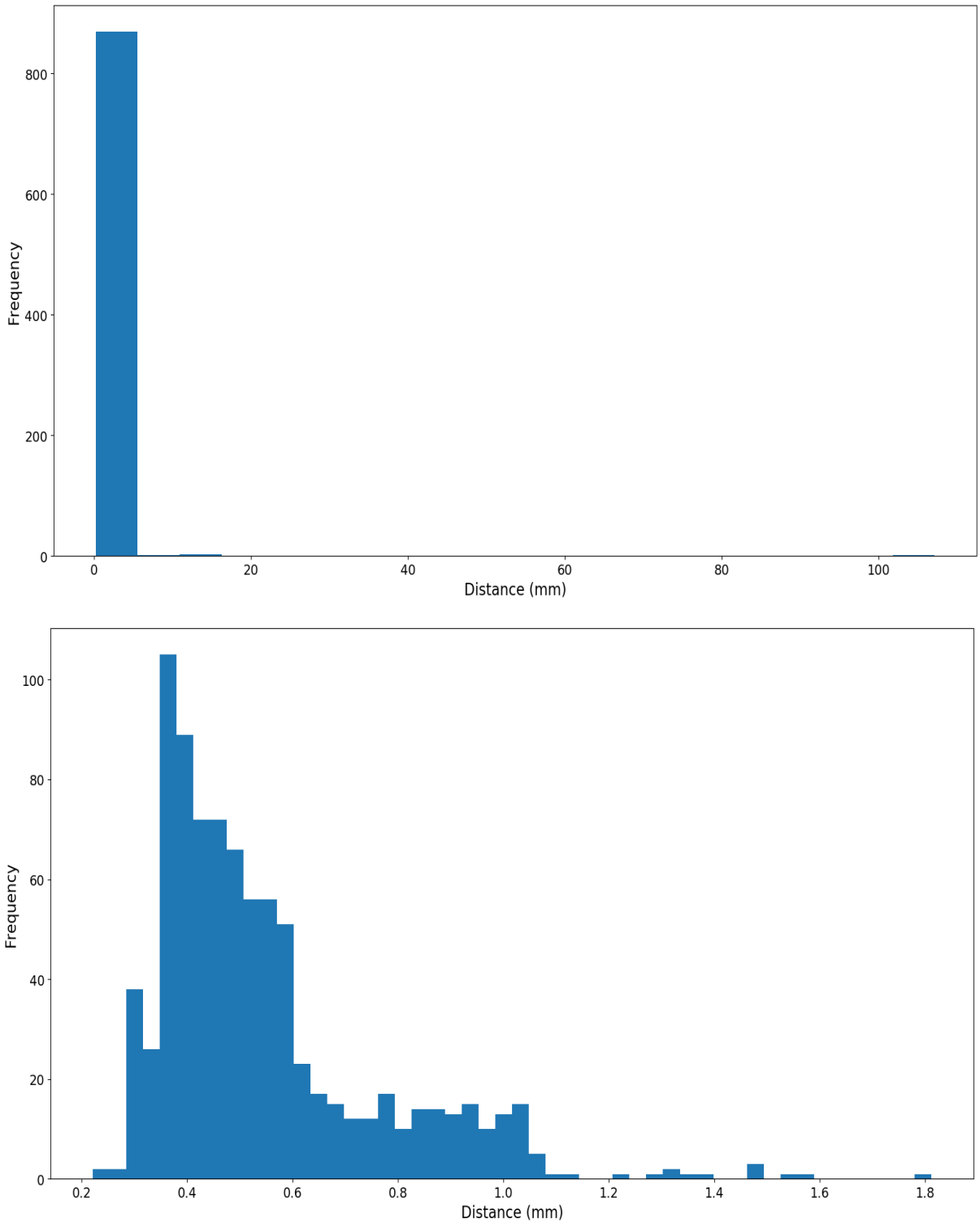

Figure 40. Distance of interaction points from nearest LUT point at apex
On the top image, the distance between the interaction point and the nearest LUT point is shown for all points. On the bottom image, only those points which were within 2mm of the nearest LUT point are shown.

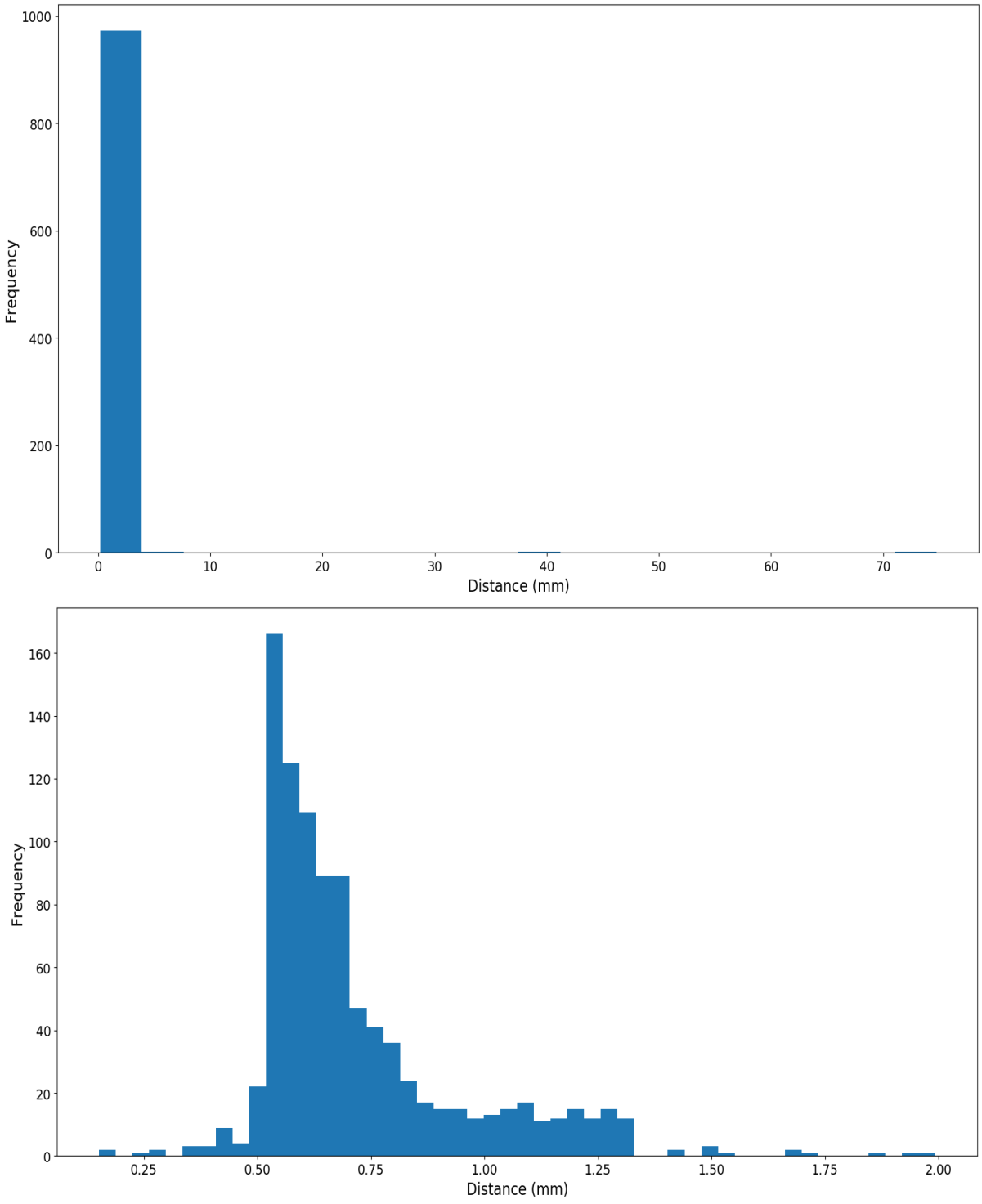

Figure 41. Distance of interaction points from nearest LUT point at central region On the top image, the distance between the interaction point and the nearest LUT point is shown for all points. On the bottom image, only those points which were within 2mm of the nearest LUT point are shown.

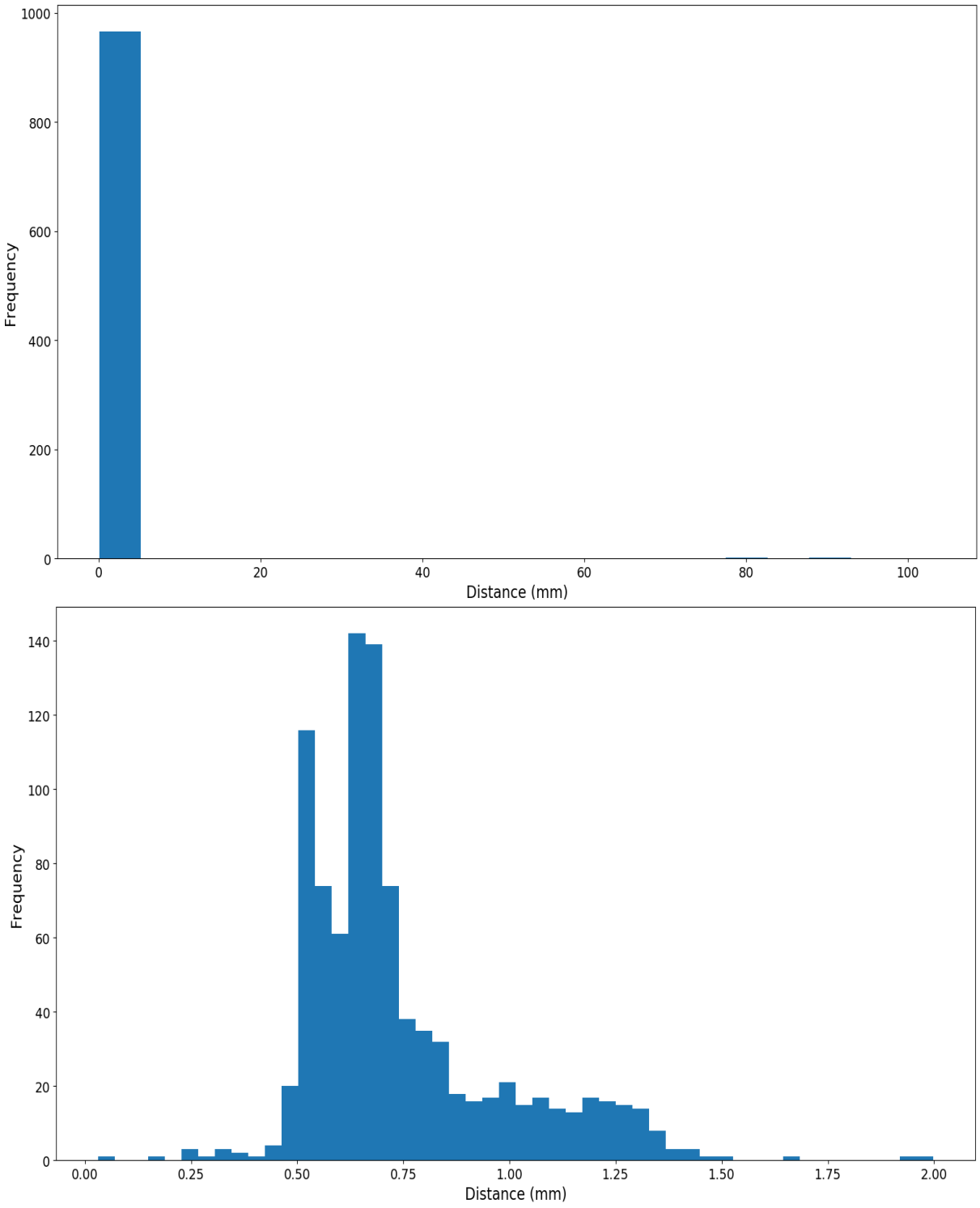

Figure 42. Distance of interaction points from nearest LUT point at base
On the top image, the distance between the interaction point and the nearest LUT point is shown for all points. On the bottom image, only those points which were within 2mm of the nearest LUT point are shown.

Table 3. Distance of gamma ray interaction points from nearest LUT point

Region	Total # of points interacted	Distance to nearest LUT point < 1.5mm	Distance to nearest LUT point < 2mm	Distance to nearest LUT point < 3mm	Distance to nearest LUT point > 3mm
Apex	881	851 (96.6%)	854 (96.6%)	862 (97.8%)	19 (2.1%)
Central	988	957 (96.9%)	965 (97.7%)	970 (98.2%)	18 (1.8%)
Base	977	956 (97.9%)	959 (98.2%)	962 (98.5%)	15 (1.5%)

Table 4. Distance of gamma ray interaction points from path of gamma ray

Region	Total # of points	Distance to path < 10^{-4}mm	Distance to path < 1mm	Distance to path < 2mm	Distance to path > 2mm
Apex	881	770 (87.4%)	829 (94.1%)	848 (96.3%)	33 (3.7%)
Central	988	864 (87.4%)	930 (94.1%)	956 (96.8%)	32 (3.2%)
Base	977	862 (88.2%)	929 (95.1%)	950 (97.2%)	27 (2.8%)

For the points that were within 2mm of the gamma ray path (96.3% to 97.2% of the points), the interpolation algorithm was used to localize the interactions. The difference between the localized point and the actual interaction of the gamma ray was recorded. Table 5 gives some statistics about each of the distributions. Note that within 2 standard deviations or about 98% of the data, our localization error was better than 3mm. In fact, at the central and base region, it was better than 2mm. Even if the gamma rays Compton-scattered, for more than 99.5% of the points which were within 2mm of the gamma ray path (so that there were LUT points nearby to compare light patterns with), the localization error was less than 3mm. The distributions are shown in Figure 43 through Figure 45. Note the different axes scales of the axes in the figures. It can be seen that in the apex, localization error and spread were higher, while in the central region, the error was the lowest and with the lowest spread.

Table 5. Localization error statistics for each region

Region	Average Loc. Error (mm)	Standard Deviation	2 std. dev. above the mean (mm)	Percentage of points within 2 std. deviations	Percentage of points with error < 3mm
Apex	1.36	0.67	2.70	98.0%	99.5%
Central	0.75	0.42	1.59	98.0%	99.8%
Base	0.88	0.52	1.92	98.6%	100%

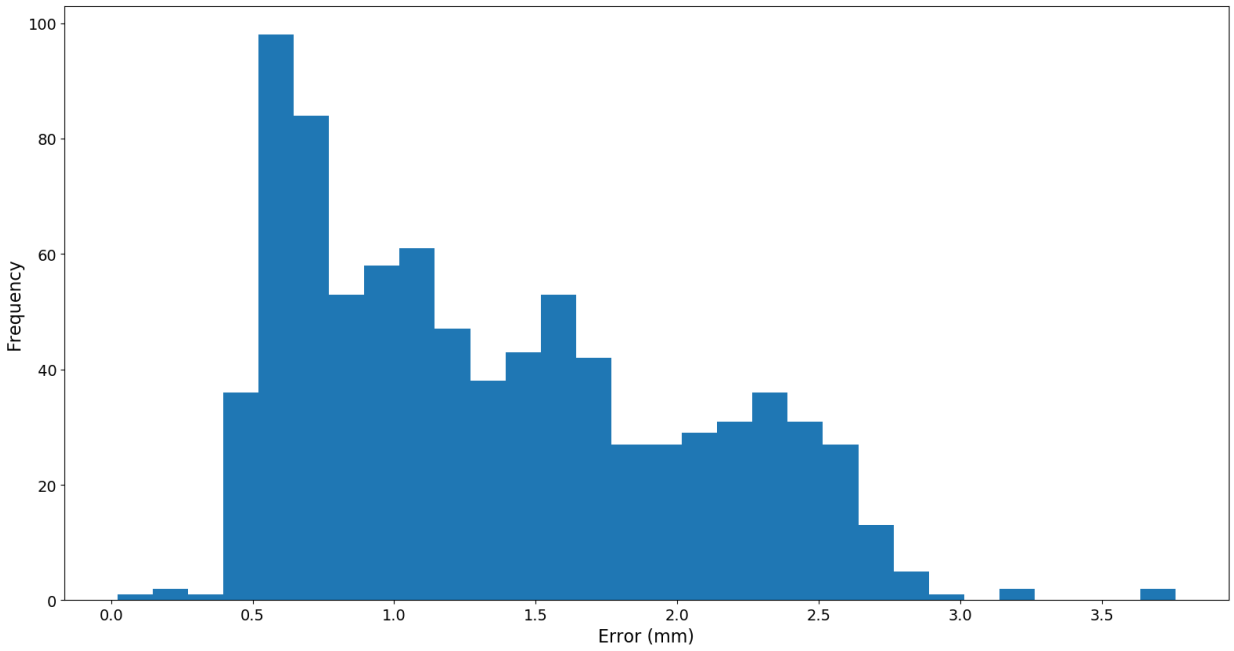

Figure 43. Absolute differences between interaction points and localized points at apex The distribution has a mean of 1.36mm with a standard deviation of 0.67mm

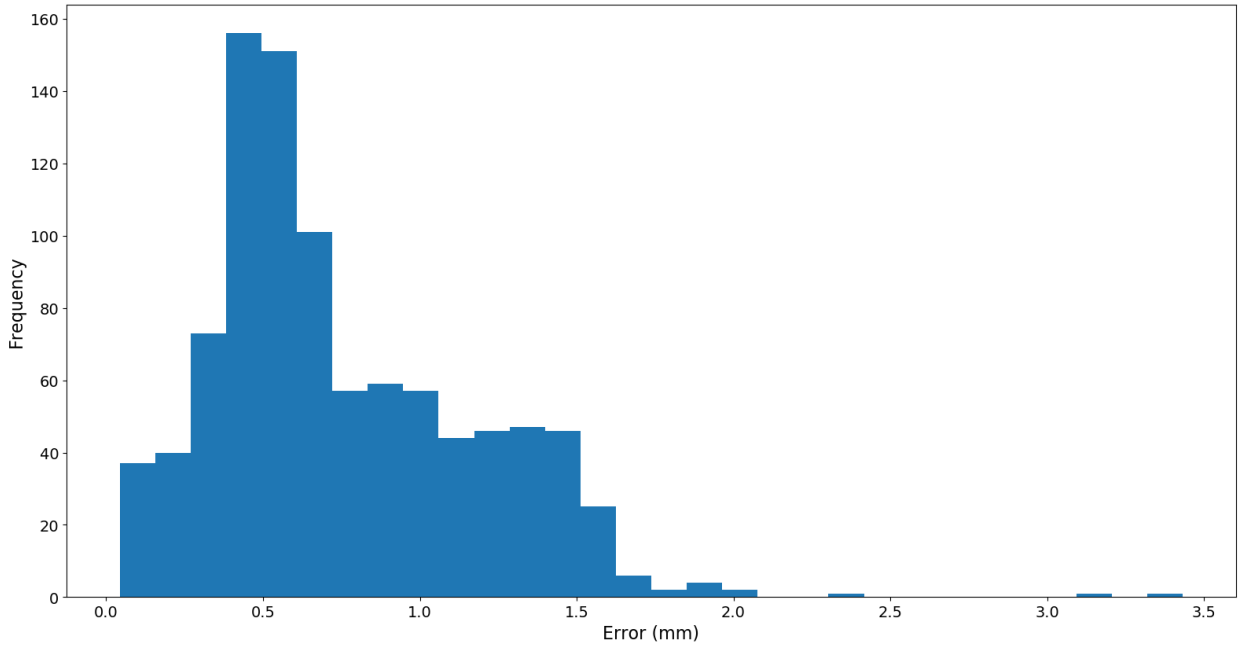

Figure 44. Absolute diff. between interaction points & localized points at central region
The distribution has a mean of 0.75mm with a standard deviation of 0.42mm

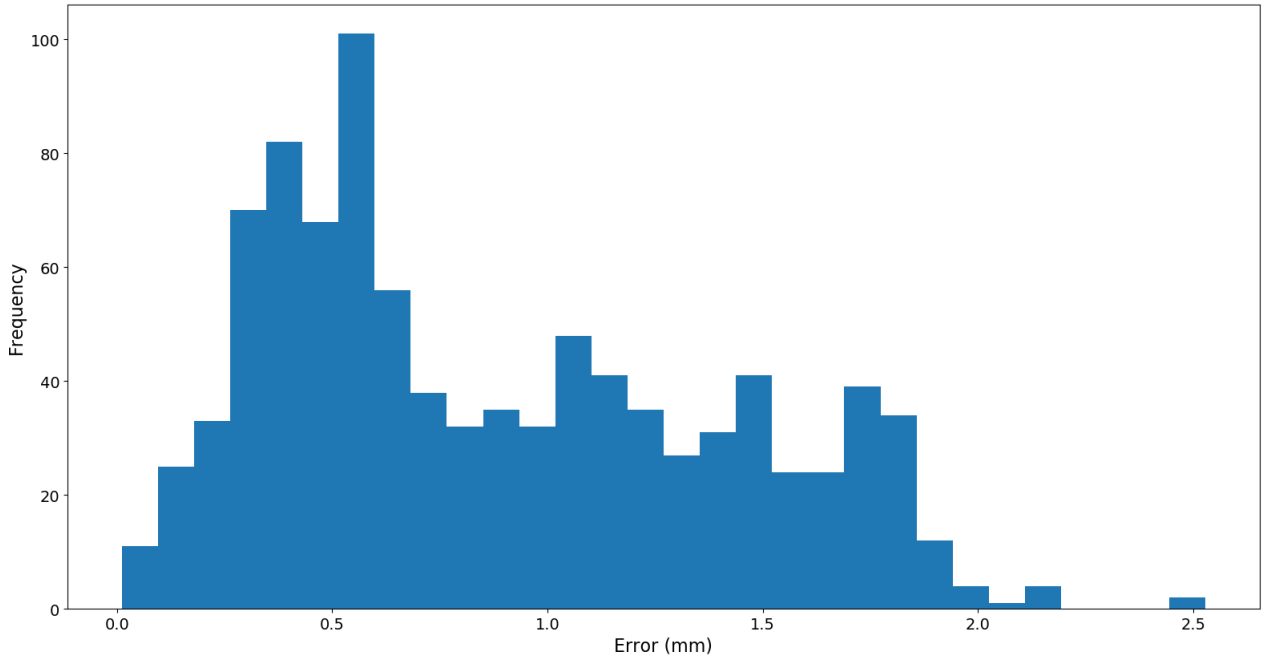

Figure 45. Absolute differences between interaction points and localized points at base
The distribution has a mean of 0.88mm with a standard deviation of 0.52mm

Chapter 6. Conclusions

By observing the 2-D light distributions, we can see that there are visual differences in the distributions between nearby points. The goal of the match and interpolation algorithms is to capitalize on these differences and obtain distinguishable digital differences from the points as well.

The results show that this is in fact feasible as most of the points in the first set of simulations matched correctly to the closest LUT point so that we are no farther than 1.0mm in most of our matches (except for points at the apex). Furthermore, the interpolation algorithm greatly reduced this error to below 0.2mm in most cases (except for at the apex and a few points at the base).

For points at the apex, we posit that there were too few bins, due to the higher curvature, to accurately be able to distinguish the light distributions of nearby LUT points. For this reason, at the apex, three out of four of the test points matched incorrectly, and the interpolation algorithm gave incorrect locations. However, since the apex is farthest from the pinhole that would be below the base of the crystal in practice, it would receive the most magnification. Thus, the poorer localization in the algorithm at the apex is curtailed by the improved magnification.

For the second set of simulations with the gamma rays, the localization algorithm worked successfully as well. For points that interacted near the set of LUT points, 98% of the localization errors were within 3mm. It is worth noting that we excluded those gamma rays which Compton-scattered far away from our generated set of LUTs. If more LUT points had been generated and more rotations used, the results of our algorithms indicate that even those gamma rays would have localized correctly (albeit they would not localize

based on the initial location of the Compton event, but based on the location of the second interaction).

The strengths of this work include the application of a robust statistical algorithm that provides accurate event localization, the usage of a novel and fast algorithm inspired by previous work (such as in PET), the fact that symmetry can be used to develop the rest of the LUT beyond one slice, and that the localization error is under 3mm. Limitations include the fact that thousands of APDs of size 2mm x 2mm would be needed to cover the crystal when built which would be costly, that scatter is unavoidable and needs to be accounted for via energy windowing (not done here), and that gamma rays were simulated from a point and not a source.

In further work, the extent to which the problem at the apex occurs needs to be examined. Perhaps devices with non-linear gain mechanisms are necessary in the apex and other, perhaps more sensitive algorithms for matching need to be explored. The entire set of points discussed in Figure 12 needs to be simulated, and test points at more regions need to be developed. The second set of simulations needs to be performed at different regions of the crystal, not just at the three regions (apex, central, base) performed here. To extend the work even further, resolution of the detector as a whole needs to be tested—that is, how close together can two points outside of the pinhole be for them to still be viewed as distinct points when the images are back-projected to the region of interest for different applications, such as Cardiac SPECT. Also, the effect on the accuracy of the algorithms using bins with larger sizes needs to be examined, so as to reduce the number of photosensors and electronics used in the final design.

Although different types of curved detectors have been used previously for PET, the novelty of this project lies in the usage of a hemi-ellipsoid crystal and its usage in SPECT. Furthermore, our algorithms centered around the LUT are unique as well. These preliminary results show the likelihood of being able to achieve 3mm localization error. With this system, it is hoped that the Cardiac SPECT system can achieve 3 times the sensitivity as current second-generation SPECT systems. The detector design and algorithm can be used in other areas of application as well, such as Brain SPECT and SPECT for small animal imaging.

Bibliography

Alexander, G. A. (2016). *Gamma Camera*. Retrieved from ScienceDirect: https://www.sciencedirect.com/topics/medicine-and-dentistry/gamma-camera

Bhusal, N., Dey, J., Xu, J., Kalluri, K., Konik, A., Mukherjee, J. M., & Pretorius, P. H. (2019). Performance analysis of a high-sensitivity multi-pinhole cardiac SPECT system with hemi-ellipsoid detectors. *Medical Physics, 46*(1), 116-126.

Carron, I. (2009, Nov 24). *CS: These Technologies Do Not Exist: A Random Anger Coding Scheme for PET/SPECT cameras*. Retrieved from Nuit Blanche: https://nuit-blanche.blogspot.com/2009/11/cs-these-technologies-do-not-exist.html

Centers for Disease Control and Prevention. (2017, Aug 23). *Heart Disease Fact Sheet*. Retrieved from Division for Heart Disease and Stroke Prevention: https://www.cdc.gov/dhdsp/data_statistics/fact_sheets/fs_heart_disease.htm

Centers for Disease Control and Prevention. (2017, Nov 28). *Heart Disease Facts*. Retrieved from U.S. Department of Health & Human Services: https://www.cdc.gov/heartdisease/facts.htm

CERN. (2018, Dec 11). *Geant4 Examples*. Retrieved from Geant4 A Simulation Toolkit: http://geant4-userdoc.web.cern.ch/geant4-userdoc/Doxygen/examples_doc/html/

Dey, J. (2010). *United States Patent No. 8519351B2.*

Dey, J. (2012, April). Improvement of Performance of Cardiac SPECT Camera using Curved Detectors With Pinholes. *IEEE Trans. Nuclear Science, 59*(2), 334-347.

Erlandsson, K., Kacperski, K., Gramberg, D. v., & Hutton, B. F. (2009, Apr). Performance evaluation of D-SPECT: a novel SPECT system for nuclear cardiology. *Physics in Medicine & Biology, 54*(9), 2635–2649.

Garcia, E. V., Faber, T. L., & Esteves, F. P. (2011, Feb). Cardiac Dedicated Ultrafast SPECT Cameras: New Designs and Clinical Implications. *The Journal of Nuclear Medicine, 52*(2), 210-217.

Gentit, F.-X. (2007, Sept 28). *Litrani*. Retrieved from Litrani: https://crystalclear.web.cern.ch/crystalclear/LitraniX/Litrani/litrani/index.html

Iwata, K., Hwang, A., Wu, M., Tang, H., Silva, A. D., Wong, K., . . . Hasega, B. (2001). Design and utility of a small animal CT/SPECT system. *IEEE Nuclear Science Symposium Conference Record (Cat. No.01CH37310)*, *3*, pp. 1849-1852. San Diego, CA.

Knoll, G. F. (2010). *Radiation Detection and Measurement.* New York: John Wiley & Sons.

Li, H. H. (1976). Refractive index of alkali halides and its wavelength and temperature derivatives. *Journal of Physical and Chemical Reference Data, 5*(2), 329–528.

Madsen, M. T. (2007, April). Recent Advances in SPECT Imaging. *The Journal of Nuclear Medicine, 48*(4), 661-673.

N. Bhusal, J. D. (2019). Performance analysis of a high-sensitivity multi-pinhole cardiac SPECT system with hemi-ellipsoid detectors. *Med. Phys., 46*(1), 116-126.

N. Grassi, G. C. (2008). PIXE characterization of CsI(Tl) scintillators used for particle detection in nuclear reactions. *Nuclear Instruments and Methods in Physics Research Section B, Beam Interactions with Materials and Atoms, 266*(10), 2383-2386.

National Institute of Biomedical Imaging and Bioengineering. (2016, Jul). *Nuclear Medicine*. Retrieved from U.S. Department of Health and Human Services: https://www.nibib.nih.gov/science-education/science-topics/nuclear-medicine

Polyanskiy, M. N. (2018, Mar 01). *Refractive index database*. Retrieved from RefractiveIndex.INFO: https://refractiveindex.info/?shelf=main&book=CsI&page=Li

Rohatgi, A. (2019, April). *WebPlotDigitizer*. Retrieved from https://automeris.io/WebPlotDigitizer

S. Agostinelli et al. (2003). Geant4 – A Simulation Toolkit. *Nucl. Instrum. Meth., A506*, 250-303.

Saint-Gobain. (2007). *CsI(Tl) Thallium activated Cesium Iodide*. Retrieved from Saint-Gobain Crystals: https://www.crystals.saint-gobain.com/products/csitl-cesium-iodide-thallium

Segall, G. M., & Delbeke, D. (2011). Status of and trends in nuclear medicine in the United States. *Journal of Nuclear Medicine*, 24S-28S.

Seo, Y., Mari, C., & Hasegawa, B. H. (2008, May). Technological Development and Advances in Single-Photon Emission Computed Tomography/Computed Tomography. *Seminars in Nuclear Medicine, 38*, 177-198.

Slomka, P. J., Pan, T., Bermand, D. S., & Germano, G. (2015, May-June). Advances in SPECT and PET Hardware. *Progress in Cardiovascular Diseases, 57*(6), 566-578.

Slomka, P. J., Patton, J. A., Berman, D. S., & Germano, G. (2009, Apr). Advances in technical aspects of myocardial perfusion SPECT imaging. *Journal of Nuclear Cardiology, 16*(2), 255–276.

Volokh, L., Lahat, C., Binyamin, E., & Blevis, I. (2008). Myocardial perfusion imaging with an ultra-fast cardiac SPECT camera - a phantom study. *2008 IEEE Nuclear Science Symposium Conference Record* (pp. 4636-4639). Dresden, Germany: IEEE.

Weik, M. H. (2000). *Lambert's cosine law. In: Computer Science and Communications Dictionary.* Boston, MA: Springer.

Vita

Hanif Rauf Soysal was born in Turkey and raised in the Unites States. He received his Bachelor of Science in Biological Engineering from Louisiana State University before continuing his education in Medical Physics at the same University. He plans to pursue a career as a clinical Medical Physicist after his residency at University of Mississippi Medical Center.